Title

Human nuclear hormone receptor activity contributes to malaria parasite liver stage development.

Journal

Cell Chemical Biology, 30(5)

Authors

Mittal, Nimisha

Davis, Chadwick

McLean, Peter

et al.

Publication Date

2023-05-18

DOI

10.1016/j.chembiol.2023.04.011

Peer reviewed

HHS Public Access

Author manuscript

Cell Chem Biol. Author manuscript; available in PMC 2024 February 20.

Published in final edited form as:

Cell Chem Biol. 2023 May 18; 30(5): 486–498.e7. doi:10.1016/j.chembiol.2023.04.011.

Human nuclear hormone receptor activity contributes to malaria parasite liver stage development

Nimisha Mittal[1], **Chadwick Davis**[2,a], **Peter McLean**[2], **Jaeson Calla**[1], **Karla P. Godinez-Macias**[1,3], **Alison Gardner**[2], **David Healey**[2,b], **Pamela Orjuela-Sanchez**[1,2,c], **Sabine Ottilie**[1], **Yolanda Chong**[2], **Christopher Gibson**[2,*], **Elizabeth A. Winzeler**[1,*,¥]

[1]Department of Pediatrics, University of California San Diego, 9500 Gilman Drive, La Jolla, CA 92093, United States

[2]Recursion 41 S Rio Grande Street Salt Lake City, UT 84101, United States

[3]Bioinformatics and Systems Biology Graduate Program, University of California San Diego, 9500 Gilman Drive, La Jolla, CA 92093, United States

Summary

Chemical genetic approaches have had a transformative impact on discovery of drug targets for malaria but have primarily been used for parasite targets. To identify human pathways required for intrahepatic development of parasite we implemented multiplex cytological profiling of malaria infected hepatocytes treated with liver stage active compounds. Some compounds, including MMV1088447 and MMV1346624, exhibited profiles similar to cells treated with nuclear hormone receptor (NHR) agonist/antagonists. siRNAs targeting human NHRs or their signaling partners identified eight genes that were critical for *P. berghei* infection. Knockdown of NR1D2, a host NHR, significantly impaired parasite growth by downregulation of host lipid metabolism. Importantly, treatment with MMV1088447 and MMV1346624, but not other antimalarials, phenocopied the lipid metabolism defect of NR1D2 knockdown. Our data underlines the use of high content imaging for host-cellular pathway deconvolution, highlights host lipid metabolism as a drug-able human pathway and provides new chemical biology tools for studying host-parasite interactions.

[*]Correspondence: chris.gibson@recursionpharma.com, ewinzeler@health.ucsd.edu.
[a]Current address: Eikon Therapeutics, Hayward, California
[b]Current address: Enveda Biosciences, Salt Lake City, Utah
[c]Current address: Novartis Institute for Tropical Diseases, Emeryville, California
[¥]Lead Contact:

Author Contributions

N.M., C.D., P.M., and E.A.W. designed the experiments and wrote the manuscript. Cell painting assays and data analysis for the same was done by C.D., A.G., D.H., P.M., and P.O.S. Y.C. conceived of and provided supervision for the Cell Painting Assays. siRNA screen, knockdown generation, infection analysis, design of RNA sequencing, design and analysis of immunofluorescence experiments was done by N.M. Image acquisition was done by J.C. Analysis of RNA sequencing and chemoinformatic analysis was done by K.G.M. C.G. provided funding and supervision of Cell Painting assays. S.O. helped with compound sourcing. E.A.W. provided funding, supervision, analyzed data and wrote the manuscript. All authors read and approved the manuscript.

Declaration of Interests

All authors affiliated with Recursion Pharmaceuticals, Inc have real or potential ownership of public equities in the company and thereby declare a potential conflict.

Keywords

Malaria; Plasmodium; Drug Discovery; Phenotypic screening; siRNA; Nuclear Hormone Receptors

Introduction

Malaria is caused by parasites of the genus *Plasmodium*. It is one of the major infectious diseases found in most of the tropical world, resulting in 228 million cases and 405,000 deaths globally (WHO report 2019).

The infectious form of the parasite i.e., the sporozoites, are transmitted to the host through the bite of infected female *Anopheles* mosquito. Within the host, sporozoites migrate through several hepatocytes before infecting the final one [1]. Once within the resident host cell, the parasite forms a parasitophorous vacuole (PV) within which it develops into the exo-erythrocytic form [2,3]. Within the PV, the sporozoite then differentiates into an active replicative form, the trophozoite. The trophozoite then enters schizogony, undergoing rapid cellular growth and multiple rounds of DNA replication. Simultaneously, it also replicates its organelles and forms a multinucleate syncytium that grows within the infected hepatocyte [4]. This period of growth varies depending on the species of the parasite. It can last for 5-7 days for *P. falciparum* while for the rodent malaria *P. berghei* it lasts for only two days. Following this, the developed merozoites enter the bloodstream to invade, multiply within, and eventually lyse red blood cells (RBCs), leading to the physiological symptoms of the infection.

In contrast to erythrocytes, human hepatocytes remain transcriptionally active after parasite infection. A metascape analysis of the 841 human genes upregulated after parasite infection done using a dual RNA-seq study, showed enrichment of phosphatidylinositol phosphate biosynthetic processes, microtubule cytoskeleton organization, RHO GTPase cycle, and lipid biosynthetic process [5]. These transcriptional changes likely support the profound morphological changes that are observed upon infection. These changes include the redistribution of Golgi and endoplasmic reticulum around the parasitophorous vacuole [6], metabolic changes needed to support the development of up to 10,000 parasite daughter cells, and potentially fundamental changes to the host secretion pathways that result in a variety of host proteins being trafficked to the parasitophorous vacuole (under review).

Although human cytological and transcriptional changes are readily observed, identifying the key human players whose modulation could lead to better therapies are more difficult. Although CRISPR and RNAi strategies [5,7–12] could reveal host proteins that are needed for parasite development, they may not reveal which proteins are “drug-able” and thus represent opportunities for therapeutic interventions with small molecules.

An alternative method to using functional genomics for druggable protein identification is via reverse chemical genetics. Here one starts with a compound that has activity and works backwards to discover the druggable target. Chemical genetics has had a profound impact on the identification of druggable targets in the malaria parasite asexual blood

stages. Compounds are first identified that block parasite growth using phenotypic screening approaches. Targets are identified from active compounds using target-deconvolution methods [13]. The parasite targets that are revealed have a development advantage in that they are considered "chemically-validated". Reverse chemical genetics could be used in liver stages as well, and indeed, compounds that prevent parasites from developing in liver stages, but which are inactive against parasite blood stages have been identified [14]. However, identifying the targets of such liver stage active compounds remain challenging. *In vitro* evolution and whole genome analysis works often for target discovery against parasite blood stages, this method will not work in liver stages because it generally depends on the ability to continuously propagate cells in the presence of compound, and liver stage infections are terminal—after the parasites leave the cell, they do not reinvade but instead move onto blood cells. In addition, the host cell is destroyed. Furthermore, proteomic approaches such as the Cellular Thermal Shift Assay (CETSA) for target discovery would be difficult, given the small number of infected cells (typically 1 in 100).

Recent technical advances in automation, microscopy, software engineering, and data science have enabled the rapid generation of omics-level cellular morphology data that are used to generate profiles that are leveraged to classify cellular states. These image-based, "cell painting" profiles, have successfully classified the cellular pathway-level activities of compounds and genes, predicted the activity of compounds across hundreds of assays, and served as the basis for chemical suppressor screens [15–19 20–23]. We hypothesized that this approach would provide clues about the pathways that are affected by the subset of liver active molecules that act against host targets.

To test our hypothesis, we developed a morphological profiling workflow. Compounds with known antimalarial liver stage activity but little or no blood stage activity [14] were examined in cell painting assays of infected HepG2 cells. Exposure of infected cells to some of our antimalarial compounds resulted in profiles that were similar to profiles of cells treated with inhibitors of the host nuclear hormone receptor (NHR) pathway. To further narrow down the list of potential candidates we used siRNAs targeting 136 different human NHR and NHR-related gene activity and then evaluated the resulting hepatoma cells' ability to support intrahepatic development of the parasite. We found that disruption of Nuclear Receptor subfamily 1 group D member 2 (NR1D2) resulted in reproducible defects in parasite development that was associated with changes in host cell lipid metabolism. Importantly, treatment with two liver-specific antimalarial compounds phenocopied NR1D2 inhibition, resulted in specific defects in host cell lipid metabolism. These data highlight the role of host cell lipid metabolism in supporting parasite development and suggest that NR1D2 may represent a druggable host target for controlling parasite infection.

Results

Assembling a library of liver-specific antimalarial compounds

To initiate our study, we selected a group of 217 compounds that primarily have activity in the liver stage, but not the asexual blood stage of the parasite lifecycle, reasoning that this collection might contain compounds acting against human targets. This set was derived from a previous high-throughput assay that was performed against *P. berghei*

liver stages [14]. In the previous screen, a set of 500,000 compounds was incubated with hepatocytes and subsequently exposed to luciferase-expressing sporozoites. Compounds that inhibited parasite development were identified based on a loss of luciferase signal after two days. Compounds were then independently sourced and tested for their ability to kill *P. falciparum* asexual blood stages, to cause host cell toxicity, and to inhibit biochemical luciferase activity. Independent tests also evaluated the compounds for activity against *P. vivax* schizonts and hypnozoites. Our test of 217 molecules (Table S1) had an average *P. berghei* luciferase IC_{50} of 2.65 μM and average *P. falciparum* blood stage IC_{50}s of >10 μM.

To further support the concept that these molecules might act via human targets, a chem-informatic analysis was performed with the initial dataset of 217, comparing them to known blood stage antimalarial compounds primarily from GSK TCAMS (12,969), GNF Malaria Box (5,609), and St. Jude's Research Hospital (1537) libraries [https://chembl.gitbook.io/chembl-ntd/]. Using the Tanimoto coefficient as a similarity metric and 85% as cutoff for cluster membership (see methods) showed that our set of 217 contained only 12 compounds that were similar to blood stage active compounds (Table S2).

Morphological profiling identifies putative host pathways targeted by antiparasitic compounds

To identify potential host pathways that could be modulated by the antimalarial liver stage active compounds, we used a Cell Painting profiling approach that has previously been used to assign targets to compounds. This high content imaging assay, which uses 6 stains to human proteins, membranes and organelles [24] was adapted to include an antibody targeting *P. berghei* HSP70, a parasite protein which is highly expressed in parasite liver stages and which has been previously used as a parasite marker in liver stage high content screens [25] (Figure 1A, 1B) (Fig S1). For our adapted assay, antimalarial compounds were added to HepG2 cells at 3 μM final concentration ~18 hours prior to infecting with *P. berghei* sporozoites. Crucially, the combination of antibody labeling, and our standard six-stain imaging protocol enabled us to screen for compounds that reduced the number of schizonts as well as those which modified host cell morphological profiles. Interestingly, and despite only a subset of cells being infected, the morphological profiles of HepG2 cells exposed to infectious mosquito salivary extract (positive control) and the same material inactivated through UV-irradiation (negative control) (Figure 1C) demonstrated a clear and significant separation of the profiles. These profiles were derived from the morphology stains mentioned in the protocol and specifically excludes the spectrally distinct, near-infrared parasite HSP70 antibody label (Figure 1C). This demonstrates the sensitivity of the approach to detect aggregate changes to cell populations that are not apparent from visual inspection of individual images.

It was expected that most of the compounds would block *P. berghei* development in liver stages, and indeed, of the 217 evaluated with the HSP70 EEF antibody label, 25 reduced exoerythrocytic numbers by ≥ 90%, 28 reduced EEF load by 70-90%, and the remaining 165 compounds reduced the load by 40-70% (Table S3). Of these 217 compounds, 73 were examined in a follow up 6-point dose response experiment (3 μM, 1 μM, 0.3 μM,

0.1 μM, 0.03 μM and 0.01 μM) which further confirmed the antiparasitic activity of these compounds.

To infer the cellular pathways modulated by the putative host-targeting anti-parasitic compounds, we compared the morphological profiles of the infected and compound-treated HepG2 cells with the profiles of infected HepG2 cells treated with a commercially available, annotated set of 90 compounds designated as the landmark set. This set is composed of compounds with well-characterized biological activity against 30 different cellular targets (Table S4) that had previously been selected to yield morphological changes in the cell painting assay.

For each cellular pathway, we aggregated the morphological profiles from three representative compounds by averaging and compared the resulting profile to that resulting from each putative anti-parasitic compound. We defined a similarity significance threshold based on the similarity distribution between the morphological profiles of the landmark compounds and unrelated cellular pathways in the landmark set. With this approach, we identified 27 putative, host-targeting, antiparasitic compounds which exhibited profiles that were similar to those of sphingosine-1-phosphate (S1P) receptor agonists, gamma-secretase inhibitors, transforming growth factor beta (TGFβ) pathway interactors, and nuclear hormone receptor (NHR) agonists/antagonists (Figure 1D). The NHR landmark class was one of the most represented classes among the active host-targeting antiparasitic molecules, we prioritized this pathway for downstream validation efforts. Although it may not be readily apparent why different agonist or antagonists of nuclear hormone receptors show similar profiles in cell painting assay, the high-level morphological changes that come from activating a transcriptional program are likely to be more similar than those observed after treating cells with a checkpoint inhibitor, or a DNA damaging agent.

RNAi Screen Identifies Nuclear Hormone Receptors of the Host Required for Liver Stage Plasmodium Parasite Infection

Nuclear hormone receptors (NHRs) comprise a superfamily of intracellular transcription factors that are key players in human cell signaling and are considered one of the most druggable of human targets because many contain binding sites for small molecules such as estrogen. NHR orthologs are not found in the malaria parasite genome. Recently, their role in the context of modulating infectious diseases has emerged [26]. Since, pharmacological interventions are available to target many NHRs for human metabolic diseases [27], identification of NHRs involved in Plasmodium infections could provide opportunities for drug repurposing. To specifically define the NHRs involved in parasite development, we conducted a small-scale RNAi screen to selectively silence the expression of 136 genes. This included siRNAs targeting the 48 NHRs known to be coded by the human genome and 71 genes coding for kinases, receptors and adaptor proteins that help in NHR signal transduction (Table S5). The remaining 17 genes included transcription factors that can either act independently or as co-activators/co-repressors with the NHRs to regulate target gene expression. Briefly, as shown in Figure 2A, siRNAs targeting each gene were pre-spotted on a 1536-well plate (three unique siRNAs per gene with two replicates per siRNA) with non-targeting siRNAs (siSEL_NTC) used as negative controls. HepG2, were reverse-

transfected for 24 hours and then infected with *P. berghei* luciferase-expressing sporozoites (*P. berghei*-Luc) [28], at a MOI of 0.3. Forty-eight hours later, the relative bioluminescence was measured (Figure 2A). In parallel HepG2 viability was determined using a Cell-Titer Glo assay that measures ATP levels. The screens were found to be highly reproducible, with a positive correlation between each replicate (Figure 2B).

For hit selection, we used two methods; two tailed t-test and strictly standardized mean difference (SSMD). SSMD allowed us to capture the mean and variability of each siRNA effect, thus providing a better measure of the strength of phenotype of a particular knockdown [29]. Genes with p value <0.05 and with SSMD score ≤ −2 (Figure 2C, Table S6) were selected as hits. A total of eight genes were identified (Figure 2D, Table 1). Downregulation of these transcripts showed a significant reduction in the liver stage parasite burden without affecting the cell viability (Figure 2E & 2F). Among the set of active siRNAs pools, two targeted the NHRs, NR3C1 and NR1D2, encoding the glucocorticoid receptor (GR) and the Nuclear Receptor subfamily 1 group D member 2, respectively. Other pools that resulted in significant decrease in parasite infection levels were AKT2, ATF4, GNAS, GPER1, GRB2 and HSPA1B.

Knockdown of host NR1D2 suppresses the intra-hepatic development of the schizonts

NR1D2 piqued our interest as our previous dual RNA-seq analysis [5] shown a significant increase (−logP = 37.60 at 48 hours) in the transcript levels of NR1D2 at 24 and 48 hours post infection (Figure 3A). NR1D2 codes for Nuclear Receptor subfamily 1 group D member 2 also known as Rev-erb beta. It acts as a transcriptional repressor regulating several physiological functions including circadian rhythm, cellular differentiation but also lipid metabolism [32]. To further understand the role of NR1D2 in context of Plasmodium infection, stable knockdowns of *NR1D2* were generated in two different hepatoma cell lines; HepG2 and HC-04. Depletion but not full ablation of NR1D2 was confirmed at the mRNA and protein levels using qPCR and immunoblotting (Figure S2). qPCR against parasite genes showed the expected decrease in *P. berghei* infection levels (as p<0.001) (Figure 3B). Interestingly, NR1D2 deficiency in the host cells did not impair the invasion of the parasite, rather it resulted in either developmental arrest or enhanced clearance of the parasites by the host cells, as there was a significant decrease in parasite load at 48 hpi and no change at 4 hpi (Figure 3C). Furthermore, high content image analysis of the infected HC-04 control shSCR and sh*NR1D2* cells revealed that although there was no change in the overall infection rate (number of hsp70 positive events) (Figure 3D), there was a significant reduction in the mean size of the exoerythrocytic forms in NR1D2 deficient cells at 48 hpi (Figure 3E), but not controls, indicating a likely developmental defect. This was further confirmed by immunofluorescence microscopy which showed schizonts in HC-04 sh*NR1D2* cells had a lower number of merozoites (Figure 3F, 3G)

NR1D2 deficient HC-04 cells showed altered transcription of genes involved in lipid metabolism

NR1D2 has been hypothesized to play a role in circadian rhythm, cellular differentiation, and also cellular metabolism. This has been studied in a variety of different cell lines and tissues. For example, RNA-seq studies of NR1D2 knockdowns in human glioblastoma cells

showed changes in genes involved in actin regulation and the epithelial to mesenchymal transition [30]. To identify the host pathways that could be regulated by NR1D2 transcription specifically in our hepatoma lines, we conducted an RNA-seq study. HC-04 sh*NR1D2* and shSCR cells were plated in 6-well plate. Forty-eight hours later, the cells were harvested for RNA extraction and sequencing. A total of 60,649 human transcripts were detected of which 13,920 had at least one sample with >10 reads. Principle component analysis showed, strong separation of the two different cell types, but the expression patterns were generally consistent across experimental replicates (R^2 0.91-0.99). Among the 239 significantly differentially expressed genes, transcripts for 164 genes were upregulated (p value <0.05, $\log_2$ fold > 1), whereas transcripts for 75 genes was downregulated (p value <0.05, $\log_2$ fold < −1) (Figure 3H) (Table S8). Gene ontology enrichment analysis using Metascape demonstrated several pathways that were modulated in response to NR1D2 knockdown (Table S9 and S10) including steroid and hormone metabolism, retinoid metabolism and glycoside metabolism (Figure 3I, Table S10). However, consistent with previous reports which had shown that NR1D2 tightly controls lipid metabolism [31]. [32] we observed that metabolism of lipid was the most significantly downregulated pathway in sh*NR1D2* cells (Log_{10} p= −7.211). Interestingly, our previous dual RNA-seq analysis of flow sorted infected hepatoma cells also [5] demonstrated an upregulation of lipid biosynthetic processes (GO:0008610 $\text{Log}_{10}(q) = -1.25$) indicating the requirement of host lipid metabolism for intrahepatic parasite development.

Recently, it was demonstrated that *Burkholderia pseudomallei*, a gram-negative bacterium, induces lipid accumulation in host lung epithelial cells upon infection through NR1D2-mediated PNPLA2/ATGL suppression [33]. To determine if we would also see changes, in the levels of lipid in infected sh*NR1D2* cells we used immunofluorescence microscopy to visualize the intracellular lipid droplets. At 48 hours post infection, we observed there was reduced staining for neutral lipids in the uninfected (Figure S3) as well as in the parasite infected sh*NR1D2* (Figure 3J) knockdown cells than the infected control. The mean fluorescence intensity (MFI) of the lipid droplets in infected sh*NR1D2* was significantly lower than the MFI of lipid droplets in shSCR cells (p< 0.0001) (Figure 3K). Taken together, our data identifies NR1D2 as a regulator of host lipid metabolism that is critical to the liver stage development of Plasmodium.

Nuclear hormone receptor modulating compounds affect lipid levels of the host

Our cell painting assay showed that MMV1088447 and MMV1346624 (Figure 4A), two compounds with liver stage activity but with little activity against asexual blood stages [14], were two compounds that phenocopied treatment with tamoxifen, endoxifen and lichochalcone A (classified as estrogen/progesterone receptor inhibitors) and were the most potent. Based on this, as well as the role of NR1D2 in promoting parasite infection we hypothesized that MMV1088447 and MMV1346624 could affect NR1D2 signaling. To test this, HC-04 cells were pretreated at 1x and 2x IC_{50} of MMV1088447 (IC_{50} :1.05 ±0.29 μM) and MMV1346624 (IC_{50}: 1.04 ± 0.73 μM), respectively, infected with *P. berghei* sporozoites and imaged after 48 hours (see Methods). In addition, we used ARN-5187 [34] a cell-permeable piperazinylmethylphenol compound that exhibits dual inhibitory activity toward REV-ERBß (NR1D2) mediated transcriptional regulation and autophagy, with an

IC_{50} of 15 μM against human NR1D2. None of the three compounds were cytotoxic to the cells, as healthy host nuclei were observed for each treatment (Figure 4B). Our hypothesis was that these compounds would give a cytological phenotype that was similar to the NR1D2 knockdown. We observed that the parasite size was smaller in cells treated with either MMV1088447 or MMV1346624, relative to DMSO controls. Similar phenotype was observed in cells treated with ARN5187. This was further corroborated by significant reduction in the number of merozoites per schizont in cells treated with MMV1088447, and MMV1346624 in dose dependent manner, relative to DMSO-treated cells ($p<0.001$) (Figure 4C). ARN5187 treated cells also had a lower number of merozoites per schizont. Consistent with our previous observation of lower lipid levels in shNR1D2 cells, there was reduced lipid levels in cells treated with our test and control compounds, confirmed by lowered staining with HCS lipid Tox stain (Figure 4B, 4D). Interestingly, we also observed reduced staining for NR1D2 in the infected cells (Figure 4E).

To ensure that the phenotype observed was specific to our test compounds and not a byproduct of parasite death we examined the lipid levels in uninfected HC-04 cells treated with several antimalarial compounds whose mechanism of action is well established, including atovaquone [35] and GNF179 [36]. We also included another compound from our screen MMV1452174 which was identified as potential modulator of the host S1P pathway. Under all tested conditions we did not observe any significant changes in the HCS lipid tox staining intensities (Figure S5A, S5B) for any compounds except for MMV1088447, MMV1346624 and ARN5187. These data also further support our hypothesis that MMV1088447 and MMV1346624 are exerting their antimalarial activity by modulating host pathways.

The cell painting assay, siRNA assays and lipid microscopy studies do not demonstrate direct inhibition of NR1D2 and our data is consistent with either compounds acting upstream of NR1D2 in the signaling cascade or inhibiting it directly. Although both compounds resulted in reduced NR1D2 staining via microscopy, direct binding cannot be excluded: the presence of a ligand can reduce NHR protein levels via the ubiquitin protease pathway. To further investigate this we performed several studies. We first evaluated the protein expression levels of NR1D2 in HC-04 cells treated with varying doses of (1x, 2.5x, 5x, 7,5x and 10x of IC50) MMV1088447, MMV1346624 and ARN5187, respectively, in the absence of infection. Forty-eight hours post treatment, cells were lysed and analyzed by western blot. We observed a dose dependent reduction in NR1D2 protein upon treatment with MMV1088447 and MMV1346624, but no changes in protein expression levels was observed with ARN5187 (Figure 4F), confirming the reduced staining for NR1D2 posttreatment via microscopy (Figure 4E). To determine if this might be at the level of transcription and verifiably upstream, transcript levels of NR1D2 were evaluated post treatment. Interestingly, no significant changes in RNA expression levels were observed (Figure S4), thus indicating that MMV1088447 and MMV1346624, may alter the levels of NR1D2 protein via post transcriptional mechanisms, which is a well-established mechanism for regulating NHR levels (reviewed in [37]

We also tested to see if there would be a parasite development IC50 shift after depleting NR1D2 via shRNA. Stable knockdown cells were treated with inhibitor, in dose response

format, infected with parasites and luciferase was measured after 48 hours. Here we did not see a significant dose response shift (data not shown), although it is possible that our shRNA knockdowns were not substantial enough to result in a clear significant dose response shift. We estimate NR1D2 protein levels are reduced by only 40 to 60% (Figure S2). In conditional knockdowns of parasite genes, we have sometimes observed that complete knockdown of protein levels is needed to see an effect. Expression of recombinant protein, beyond the scope of this study, will be needed to address this.

Discussion

Recent advancements in computational processing power and the field of data science have enabled the capture and interpretation of many types of data previously thought intractable [18,38–40]. In this work we have utilized these advancements to demonstrate that cellular images, with no pathway or disease-specific labeling, can be used to predict the mechanistic activity of compounds. The presented work is a case study example for malaria and the identification of host pathways that can be targeted to prevent parasite development in host cells. One of the substantial advantages of using this workflow to screen for antimalarial drugs is the in-depth analysis of the host cell status upon infection as well as upon compound treatment to identify cellular pathways impacted , thus overcoming a major limitation of phenotypic screening.

The compounds used here were carefully selected from a screen of >500,000-small molecules, based on their ability to specifically inhibit the liver stage development of the parasite but which showed little activity against the asexual blood stage [14]. Although some of these could affect parasite targets that are only needed during hepatic development, given the conservation of processes, such as protein biosynthesis and DNA replication in both liver and blood stages, this is less unlikely. In addition, the compounds described here also affected host cell morphology in the cell painting assay.

There are only few reports that highlight the importance of host specific NHRs like PPARγ [41] and VDR [42] in regulating malaria infection and to our knowledge: the role of NR1D2 has not been investigated. Due to the lack of identified physiological ligands, nuclear receptor REV-ERBβ (NR1D2) belonged to the category of orphan nuclear receptor until recently when heme was identified to bind with the ligand binding domains of this receptor in a stoichiometric ratio of 1:1 [43]. NR1D2 is known to regulate diverse physiological processes like inflammatory responses [44], glucose homeostasis [32,45]. In hepatocytes and skeletal muscles, it is known to regulate lipid metabolism [32,46]. Several genes involved in lipid metabolism like *Fatty acid translocase* (*Fat/CD36*), *Fabp3 Fabp4, etc.* were identified as NR1D2 target genes by expression of a dominant negative form of REV-ERBβ lacking the LBD in skeletal muscles [32]. Previous studies have shown that NR1D2 can regulate lipid metabolism in hepatocytes through inhibition of the PI3K-AKT pathway [30,47–49] or the sterol regulatory element binding protein 1c (Srebp-1c) and its target gene, fatty acid synthase (FAS)[50]. Plasmodium liver forms are auxotrophic for several nutrients including lipids like cholesterol and phosphatidylcholine [51]. The parasite is also known to manipulate the host's liver lipid metabolism pathways by inducing hyperproteinemia, hypertriglyceridemia, hypoglycemia, and hypocholesterolemia [52].

Drugs that target pathogen molecules are associated with resistance acquisition because of the rapid rate of parasite replication compared to the human [53]. In contrast, targeting host molecules/pathways should have less of a resistance liability. Several such host-based interventions have already been proposed against several pathogens (reviewed in [54]). Identification of host factors required for the hepatic and erythrocytic Plasmodium stages of malaria have opened opportunities for host-targeted interventions against this disease as well [27,55]. For example, targeting host aquaporin 3 leads to the elimination of *P. vivax* hypnozoites from *P. vivax* infected hepatocytes [56].

Although it is considered challenging to target host proteins for infectious disease treatment, agonists and antagonists of nuclear hormone receptors are one of most common class of human drugs. Although inhibition of some NHRs can produce severe side effects (e.g. premature menopause from tamoxifen for breast cancer), inhibition of others may not: In fact, although NR1D2 does appear to be needed for parasite development, it does not appear to be essential for mammalian life: Homozygous deletion of NR1D2 in mice did not cause overt gross abnormalities, lethality or infertility, although disruptions in NR1D2 do cause changes in circadian behavior [45] However, given the fact that NHRs are often differentially expressed in different tissues and different compounds can be directed to different organs means that a NR1D2-inhibiting antimalarial that accumulates in the liver might not necessarily cause sleep disruptions. However, there are obvious difficulties with host-targeted therapies, including toxicity. On the other hand, if a drug is to be used short term, this might be less of a concern.

Our study highlights the use of morphological profiling for identification of druggable host cellular pathways. Two compounds identified as potential host NHR modulators: MMV1346624 and MMV1088447 were used to assess their impact on the development of the parasites. Though the compounds phenocopied knockdown of shNR1D2 in cells by altering it's stability, further studies are needed to validate the direct targets of these compounds. Owing to the growing collection of small-molecule drugs available to modulate the activities of NHRs in the treatment of diseases like cancer, diabetes, or multiple sclerosis [57,58], it is increasingly likely that identifying repurposable drugs for malaria treatment is a real possibility, thereby reducing the overall time for drug discovery and development.

The phenomics approach used here identified a nuclear hormone receptor (NHR) pathway with the highest enrichment score, followed by the Sphingosine 1-phosphate (S1P) receptor pathway. S1P pathway dysregulation has previously been associated with malaria pathogenesis [59]. Other host pathways that were represented included MTH1, Histamine receptor pathway, TGF-b, gamma secreatase and reverse transcriptase. Not much is known about how these pathways are implicated in parasite development. Thus, our findings contribute to the diversity of novel host pathways that can be further explored to understand the complex host pathogen signaling as well as for antimalarial drug discovery.

Finally, our predictive ability is driven through comparing the morphological profiles of one set of compound-treated cells to another set of compound-treated cells, but such an approach is limited by the number of compounds, the diversity of their activities, and the quality of their annotations. We anticipate that the addition of new functional target classes to our

landmark library will enable the elucidation of a greater diversity of chemical activities and hence identification of novel host pathways that remain unexplored. The principles and techniques demonstrated here can be applied to any other perturbation that interacts with cells, across multiple therapeutic areas, and various stages of the drug discovery process.

Limitations of the study

Due to the unavailability of a biochemical assay to measure NR1D2 activity, it is challenging to establish MMV1088447 and MMV1346624 as direct inhibitors of this nuclear hormone receptor. Additionally, we did not see any differences in the IC50s of MMV1088447 and MMV1346624 in NR1D2 knockdown lines relative to wild type cells. Given the complex and dynamic cellular signaling these proteins are involved in, there could be likely other targets along the NR1D2 signaling axis that are contributing to dysregulation of lipid metabolism upon treatment with these compounds.

Significance

Most antimalarial chemotherapy is directed against parasite targets. However, it is likely that parasites require host factors to develop, particularly in hepatic stages. Here we use a cell chemical biology approach to search for targets and pathways that may be active during hepatic stage development. We developed and applied a morphological profiling workflow that, in a single assay, evaluates compounds for both their ability to prevent EEF development and inform on their potential cellular pathways of action. Cellular profiles of compound-treated hepatocytes exhibited profiles similar to those of nuclear hormone receptor (NHR) agonists/antagonists. Using siRNA screen we then identified NR1D2 as one of the host NHR whose knockdown is significantly impairing parasite growth by downregulation of host lipid metabolism. We also assessed the effect of the identified NHR modulators MMV1088447 and MMV1346624 on the hepatic growth of the parasites. Both compounds phenocopied the lipid metabolism defect of NR1D2 knockdown. Our data identifies NR1D2 as a druggable target for malaria prophylaxis and reveals insights about the lipid metabolic pathway that is needed to support parasite hepatic development.

STAR Methods

RESOURCE AVAILABILITY

Lead Contact—Further information and requests for resources and reagents should be directed to and will be fulfilled by the lead contact, Elizabeth Winzeler (ewinzeler@health.ucsd.edu).

Materials Availability—Cell lines generated in this study are available upon request. Depending on the reagent and institution of origin, an MTA might be required.

Data and Code Availability

- Data: Raw data from the primary siRNA screen are available upon request to the Lead Contact. Analyzed data can be found in Table S6. Raw RNA sequencing files are deposited in the short read sequence archive (http://www.ncbi.nlm.nih.gov/sra) under BioProject ID PRJNA787651.

- Code: This paper does not report original code.
- Any additional information required to reanalyze the data reported in this paper is available from the lead contact upon request.

EXPERIMENTAL MODEL AND SUBJECT DETAILS

Parasite cell lines and culture—*Plasmodium berghei* ANKA-luciferase sporozoites were isolated from infected *Anopheles stephensi* raised at UCSD.

Cell lines—HepG2-A16-CD81EGFP cells stably transformed to express a GFP-CD81 fusion protein [60], and HC-04, were cultured at 37°C and 5% CO_2 in DMEM (Life Technology, CA) supplemented with 10 % FBS, 0.29 mg/mL glutamine, 100 units of penicillin, and 100 μg/mL streptomycin. Screening media, DMEM without phenol Red (Life Technology, CA) supplemented with 5% FBS, 1.45 mg/mL glutamine, 500 units of penicillin, and 500 μg/mL streptomycin were used for the siRNA screening assay.

METHOD DETAILS

Chemoinformatic analysis of the library—A chemoinformatic analysis was performed with the initial dataset compared against a total of 30,777 known antimalarial compounds primarily from GSK TCAMS (12,969), GNF Malaria Box and liver stage (5,609), MMV Biofocus 500 (10,112) and St. Jude's Research Hospital (1537) libraries [https://chembl.gitbook.io/chembl-ntd/]. To identify similar scaffold families, a clustering analysis using Rdkit (RDKit: Open-source chemoinformatics; http://www.rdkit.org) was performed using Tanimoto as a similarity metric with 85% as the cutoff for cluster membership.

Compound Preparation—Compounds diluted in DMSO were pre-spotted on 384-well plates (Greiner Cat# 781948) in dose response (3 μM, 1 μM, 0.3 μM, 0.1 μM, 0.03 μM and 0.01 μM) using an Echo555 (Labcyte). Twenty-four hours prior to infection, HepG2 cells in assay ready format were thawed into DMEM (Thermo Fisher Cat# 11995081) supplemented with 5% heat inactivated FBS (Thermo Fisher Cat# 16000044) and 5x pen/strep (Thermo Fisher Cat# 15140122) and seeded at a density of 3500 cells/well in 50 μL.

Mosquitoes and Parasites—*Anopheles stephensi* mosquitoes were reared at 26°C and ~75 % relative humidity with 12-hour cycles of alternating light and darkness. Mosquitoes were fed with 0.3 % sucrose solution on cotton pads for routine maintenance. Mosquitoes were infected with *P. berghei* ANKA GFP-Luc-SM_{con} by feeding directly from parasite-infected mice (anesthetized with KetaVed and Xylazine). Briefly, female Swiss Webster ~ seven-week-old mice were infected by i.p. injection of parasitized blood (approximately 200 μl of blood at 5 % parasitemia), and infections were monitored by examination of Giemsa-stained tail blood smears. At 3-4 days post-infection, anaesthetized mice were exposed to cages containing ~200 starved female anopheline mosquitoes. A second blood feed was done two days later to make sure that all the mosquitoes were fed. Blood-fed mosquitoes were maintained on 8% (w/v) sucrose, 0.05% (w/v) p-aminobenzoic acid at 20 °C and 70% relative humidity. Twenty-three days post-feed, the infected mosquitoes were used for sporozoite extraction using the method described previously [14]. All animal handling was

conducted according to the UCSD Institutional Animal Care and Use Committee-approved protocols.

Sporozoite Infection—Sporozoites were extracted from the infected *A. stephensi* in complete media supplemented with an anti-mycotic cocktail consisting of 0.5 μM posaconazole (Cayman Chemical Cat# 14737), 12 μM 5-fluorocytosine (Cayman Chemical Cat# 11635), 110 μM neomycin (Sigma Cat# 1876-25G) and 50 μg/mL gentamicin (Thermo Fisher Cat# 15750-060) was used to dilute the sporozoites to 200,000/mL. Prior to infection, an aliquot of diluted sporozoites was subjected to crosslinking set to 5000x10^6 power using a UV Stratlinker 2400 (Stratagene) to inactivate the sporozoites resulting in an irradiated control. The cells were infected at a 1:2 ratio with either live sporozoites or the irradiated control and centrifuged for 3 m at 300 g prior to being placed in the incubator.

Staining—The cells were stained with a modified cell painting protocol [7]. In the modified protocol, 15 μL of 0.5 mg/mL Mitotracker Deep Red (Thermo Fisher Cat# M22426) diluted in 1% BSA (VWR Cat# 103219-874) in 1xHBSS (Thermo Fisher Cat# 14065-056) was added to the 50 μL of media in each well for 35 min. The cells were fixed with 2.13% PFA (Fisher Scientific Cat# 50980488) for 35 min followed by 3x 70 μL washes, leaving 10 μL residual volume each time, in wash buffer consisting of 0.02% sodium azide (VWR Cat# AA14314-36) in 1x HBSS. Cells were permeabilized in 60 μL 0.1% Triton X-100 (Fisher Scientific Cat# AC215682500) in 1x HBSS for 35m, followed by another 3× wash in wash buffer. Twenty μL of 3% BSA in 1x HBSS was used to block the cells for 30m, and the cells were incubated at 4°C overnight with 0.2 μg/mL *Py*HSP70 antibody [25] in 1% BSA in 1x HBSS. Following overnight incubation, the cells were washed 3×70 μL in wash buffer, leaving 10 μL residual volume, and 20 μL of secondary stain mix was added to the wells for 2.5h. The secondary stain mix consisted of the following components: 7.5 μg/mL Hoechst 33342 (Thermo Fisher Cat# H3570), 75 μg/mL Concanavalin A Alexa Fluor 488 (Thermo Fisher Cat# C11252), 4.5 μM SYTO 14 Green Fluorescent Nucleic Acid Stain (Thermo Fisher Cat# S7576), 2.3 μg/mL Wheat Germ Agglutinin Alexa Fluor 555 Conjugate (Thermo Fisher Cat# W32464), 1.5 Units/mL Alexa Fluor 568 Phalloidin (Thermo Fisher Cat# A12380) and 15 μg/mL Goat anti-Mouse IgG Secondary Antibody Alexa Fluor 750 (Thermo Fisher Cat# A-21037). A final 6× 70 μL wash cycle was conducted, and plates were sealed with 50 μL of wash buffer in the wells.

Imaging and Feature extraction—Images were acquired with an IXM microscope (Molecular Devices) using a 4x4 grid to maximize imaged area. Imaging channels are as previously described [24] with the addition of a Cy7 near-IR channel to image the schizonts. The images were segmented, and features extracted using the supplemental Cell Profiler pipeline file. Two primary objects, nuclei and schizonts, were identified using the Hoechst and Cy7 antibody staining, respectively, and secondary objects were identified using the SYTO 14 staining. Approximately one thousand features were extracted from the segmented objects and either analyzed at the cell-level directly for schizont filtering and evaluation or averaged up to the site-level for the morphology analyses.

Cellular target inference through morphological profiling

Construction of the "landmark" compound set: A set of 1415 compounds with 150 commercially annotated cellular targets (Selleck Bioactive) were applied to four different cell types (HUVEC, U2OS, Fibroblasts, RPE) in 384-well plates at 0.3, 1.0, and 3 μM in triplicate. We constructed morphological profiles for each well treatment as described previously, then averaged across all wells of a given compound to get compound profiles. We chose an initial set of 130 cellular targets for which there were at least three representative compounds per target. For targets with more than three representative compounds, we selected the three compounds whose morphological profiles were most similar to the mean morphological profile of all representative compounds. We then applied these 390 compounds alongside the putative anti-parasitic compounds in HepG2 cells, and further selected as the Landmark Set the 30 cellular targets (90 compounds) (Table S5) such that for each target, the three representative compounds produced more phenotypic similarity between themselves than 99% of an empirical null distribution consisting of many draws of three random landmark compounds. Similarity was measured as the mean angle between the profile vector of a representative compound and the mean profile of all other representative compounds.

Target inference of putative anti-parasitics—To infer the targets of the putative anti-parasitic compounds, we compared the morphological profiles of infected HepG2 cells exposed to the compounds with landmark profiles representing the 30 targets described above. Similarity between query compounds and landmarks were measured via pairwise angles between the compound vectors and the landmark vectors and resulted in a distribution of similarities for each compound. Significant similarity (or dissimilarity) was established by empirical thresholds measured from a pair-wise cosine angle "null" distribution of all landmark compounds against all landmark vectors, excluding self-pairs. Owing to an observed partial dependence of angle-to-landmark similarity on cell-count, similarity thresholds were conditioned on the mean cell density of the treated wells (Figure S8). Thresholds for upper (dissimilar) and lower (similar) cosine angle bounds were calculated with a rolling window (bin width: 100) and used the 99^{th} and 2.5^{th} percentiles, respectively. Importantly, it is only the lower-bound threshold that determines significant similarity for landmark association, and which was used to identify the most similar compound-target pairs for further investigation. The choice of the landmark compound vs. landmark vector null distribution was intended to most realistically approximate the distribution of pairwise angle similarities that could be expected between morphological profiles of unrelated compounds.

Schizont analysis

Object cleanup: Though we developed an imaging and segmentation strategy that identified schizonts with high recall, it also inappropriately segmented a non-negligible amount of debris and imaging artifacts that confounded efforts to determine the true frequency of viable schizonts in an image. This had the undesired effect of reducing the signal-to-noise ratio between our positive and negative control populations. We addressed this by using logistic regression to identify real schizonts in the two control populations based on well-level control labels (i.e., segmented objects in the irradiated-control wells are

false, and objects in the positively-infected control wells are true). This weakly supervised logistic regression method had an effect similar to a fixed baseline subtraction approach, but the pseudo-baseline was learned from the training data as opposed to being prescribed by a prior of empirical, manually annotated object counts. Once trained on the control populations, schizont objects were predicted for the remainder of the experiment and the net result was a reduction in spuriously segmented cellular artifacts, a concomitant increase in the signal-to-noise ratio between the control populations, and an increased ability to resolve schizont count reductions in query populations.

Identifying schizont-reducing compounds—To mitigate the high variance observed in the frequency of schizonts in infected cell populations, schizont counts were averaged across all sites in a well and all replicate wells in an experiment (typically 6). However, control populations were intentionally over-represented on each experiment plate by roughly 5-fold. As such, we constructed schizont-count distributions for both control populations by sampling a comparable number of wells from the control groups and averaging the results. We then established a count threshold for identifying schizont-reducing compound “hits” as the maximum of either an odds ratio of 0.9 that an observed count was part of the negative control distribution or the fifth percentile of the positive control distribution. Notably, all but one experiment had sufficient separation between the control distributions after object cleanup to use the fifth percentile as our hit selection threshold.

Hit prioritization and selection—Compound selection and advancement was based on reducing schizont frequency and having a positive landmark association. From the primary screen of 217 compounds, we identified 72 compounds that had morphological profiling and/or schizont suppressing activity. Using the before mentioned selection criteria, these compounds were advanced and assessed in dose response confirmation experiments. Twenty-seven compounds with landmark activity were identified, four of which had an NHR-like profile.

siRNA Design and Screening Controls—siRNAs targeting the various nuclear hormone receptors and their effector proteins were purchased from Thermo Fisher Scientific. Each gene was targeted by using three distinct siRNAs. There were two replicates per siRNA in each plate. Negative control samples included cells transfected with a negative control siRNA not targeting any annotated genes in the human genome. A full list of gene names and siRNA ID numbers are shown in Table S5.

High-Throughput Screening of P. berghei Infection—Twenty-five nL of the 4 μM stock siRNA were pre-printed into PDL/collagen coated Greiner Screenstar 1536 plates. On the day of assay, Lipofectamine™ RNAiMAX Transfection Reagent (Invitrogen, Cat# 13-778-030) was diluted to a final concentration of 1% in Opti-MEM (Invitrogen, Cat# 31985062). Two μl of this mixture was dispensed into each well of pre-spotted plates using MultiFloTM Microplate dispenser (BioTek). The siRNA-Lipofectamine mixture was allowed to sit at RT for one hour. HepG2-A16-CD81 cells (1500 per well) in 8 μl of antibiotic free medium were then added using the microplate dispenser. Transfection was allowed to continue for 24 hours, before the medium was replaced with 5ul of screening

medium (phenol red free DMEM + 5% PSG +5 % fetal bovine serum). Forty-eight hours after changing the medium, P. *berghei* sporozoites (*P. berghei* ANKA GFP-Luc-SM_{con}) freshly obtained by dissecting salivary glands of infected *Anopheles stephensi* mosquitoes were added to each well at a density of 1 x 10^3 per well. The plates were centrifuged for five minutes at 330g on normal acceleration and brake settings and incubated at 37°C. Forty-eight hours post infection, 2 μL of luciferin reagent (Promega BrightGlo) was added to each well and luciferase activity was detected using a Perkin Elmer Envision plate reader. In parallel, plates were processed without sporozoites for assessing the effect of siRNAs on HepG2 viability. Here Promega CellTiter Glo (2 μL) was added instead of BrightGlo.

Gene Knockdowns: lentivirus production and transduction of target cell lines—The oligos for shRNAs targeting *NR1D2* (shRNA ID: TRCN0000022192) and the non-coding controls were obtained from Eton Biosciences. The oligos were cloned in pLKO.1-puro vector (Addgene). Clones with the correct sequence insert were confirmed by sanger sequencing. For lentiviral production, Lenti-X 293T cells were co-transfected with shRNA vector and envelope plasmid, psPAX2 and packaging plasmid, pMD2.g. After 36 and 72 hours of transfections, virus particles were collected and filtered through a 0.45 μm syringe filter. Aliquots were stored at −80°C for later use.

For generating stable knockdowns HepG2-A16-CD81EGFP and HC-04 cells were plated at a density of 150,000 cells per well in a 6-well plate, 24 hours prior to viral transduction. On the day of transduction, complete media was supplemented with 10 μg/mL Polybrene® (Cat# sc-134220) and virus was added to the cells. The cells were incubated overnight at 37°C. Twenty-four hours later, media was replaced with complete media without Polybrene and cells were further incubated overnight. Cells were then split 1:2 in complete media supplemented with 1.5 μg/mL puromycin. After seven days of selection, knockdown efficiency was confirmed by qRT-PCR and immunoblotting.

RNA Isolation and Quantitative RT-PCR—To quantitate the gene expression levels in transduced cells, 1×10^6 transduced cells were dissociated using TrypLE (Gibco, Cat #12605-010). The cells were washed once with 1X PBS and total cellular RNA was extracted using RNeasy Plus Mini Kit (Qiagen, Cat# 74134), according to the manufacturer's protocol. cDNA was synthesized from 2 μg of total RNA using SuperScript™ First-Strand Synthesis System for RT-PCR (Invitrogen, Cat# 11904018), following manufacturer's instructions. 50 ng of the cDNA was used to set up qPCR reaction using SYBR green master mix (Life Technologies, Cat# 4309155).

To quantitate the expression of NR1D2 posttreatment, 2.5×10^5 cells per well were treated with varying concentrations of MMV1088447, MMV1346624 and ARN5187, respectively, for 48h. The cells were harvested and RNA extraction for qPCR was done as mentioned above.

The primer sequences are listed in Table S7.

Immunoblotting—Transduced HepG2-A16-CD81EGFP and HC-04 cells (~ 1×10^6) were trypsinized, washed once with cold 1X DPBS and then lysed in 100 μL of Pierce™

RIPA Buffer (Thermo Scientific) containing 1X cOmplete™, Mini, EDTA-free Protease Inhibitor Cocktail (Sigma Aldrich, Cat# 11836170001) and 1 mM of phenylmethyl sulfonyl fluoride. Total protein concentration was measured using the DC Protein Assay kit (Bio-Rad). Twenty μg of proteins were resolved by SDS-PAGE and transferred to nitrocellulose membranes (Bio-Rad #1704271), blocked in 5% (w/v) Blotting-Grade Blocker (Bio-Rad, Cat# 170-6404) for one hour and probed with respective primary antibody (dilution used 1:1000). HRP-linked anti-mouse or anti-rabbit (Cell Signaling Technology) were used as secondary antibodies (dilution used 1:2500). The HRP signal was visualized with SuperSignal™ West Femto Maximum Sensitivity Substrate (Thermo Scientific, Cat no: 34095) using Syngene G-Box imager. Protein levels were calculated relative to vinculin. Primary antibodies used in the study are: anti-NR1D2 (Sigma-Aldrich, cat # HPA054798) and Vinculin (Cell Signaling Technology, Cat # 13901S).

To quantitate the protein expression levels of NR1D2 posttreatment, 2.5×10^5 cells per well were treated with varying concentrations of MMV1088447, MMV1346624 and ARN5187, respectively, for 48h. The cells were harvested and lysate for immunoblotting was prepared as mentioned above. Protein levels were calculated relative to beta actin. Primary antibodies used in the study are: anti-NR1D2 (Sigma-Aldrich, cat # HPA054798) and beta actin (Cell Signaling Technology, Cat # 4967S).

Quantification of EEF development by qRT-PCR—HepG2 and HC-04 cell lines stably transduced with sh*NR1D2* and shSCR, respectively, were seeded in 24-well plate at a density of 9.0 x 10^4 cells/well. Twenty-four hours later, *P. berghei* sporozoites obtained by dissecting salivary glands of infected *Anopheles stephensi* mosquitoes were added to each well at a density of 4.5 x 10^4 per well (MOI 1:2). Two hours post infection, the cells were washed, and fresh media was added. Forty-eight hours later, the cells were harvested from each well, pellets were washed with 1X PBS and stored at −80°C until further processing. Total RNA was isolated from the pellets of infected and uninfected cells using RNeasy Plus Mini Kit (Qiagen, Cat# 74134), according to the manufacturer's protocol. cDNA was synthesized and qRT-PCR was set up as described above. The primer sequences are listed in Table S7. Infection levels were estimated by calculating the relative amounts of PbA mRNA against the Hypoxanthine Guanine Phosphoribosyltransferase (HPRT) housekeeping gene. To differentiate between impaired invasion vs developmental arrest or enhanced clearance of the parasite, HC-04 cell lines stably transduced with sh*NR3C1* and shSCR, respectively, were seeded and *P. berghei* sporozoite infection was done as described above. Samples of infected and uninfected cells were harvested at four hours post infection and 48 hours post infection. Total RNA isolation, cDNA synthesis and qRT-PCRs were set up as described above.

High Content Imaging—The high-content imaging experiments were performed as previously described [25]. Briefly, HC-04 shSCR and sh*NR1D2* cells were seeded in 384-well plates (4000 cells per well). Twenty-four hours later the cells were infected with Pb-Luc rodent malaria parasites at an MOI of 1:1. Forty-eight hours post infection, the cells were fixed by addition of paraformaldehyde (1% final formaldehyde concentration), membranes were permeabilized with 0.5% Triton-X-100 (Thermo Fisher Scientific) and EEFs were

stained using a mouse polyclonal serum raised against the Plasmodium heat shock protein 70 (PyHSP70). The EEFs were counterstained with Rhodamine Red™-X (RRX) AffiniPure Goat Anti-Mouse IgG (Jackson Immuno Research, cat# 115-295-071) and the nuclei were stained with DAPI (Vector Laboratories, cat# H-1500-10). Stained EEFs and the nuclei were then imaged and quantified using the Operetta Confocal High Content Screening System, Harmony software v3.5 (PerkinElmer, Waltham, USA). Images were captured using 10x objective. Percent infection (number of hsp70 events/ total number of nuclei) and the average parasite size (EEF area in μm^2) per well was then determined and compared to the shSCR control cells.

Plasmodium EEF nuclei quantification and imaging—Sixteen thousand cells per well of HC-04 sh*SCR* and HC-04 sh*NR1D2* were individually seeded in poly L-lysine precoated 8-well chamber slides. Twenty-four hours later the cells were infected with *P. berghei* Luc sporozoites at a MOI of 1:1 (cells/sporozoites). At 48 hpi, the cells were fixed with 1% paraformaldehyde-PBS (Affymetrix) for 20 min at room temperature, permeabilized with 0.1% tritonX-100 (SIGMA) for 10 min at room temperature, blocked with 1% bovine serum albumin and stained overnight at 4 °C using two antibodies. The first antibody was UIS4 (*Plasmodium berghei* UIS4) goat polyclonal antibody (dilution 1:1000 from a 2 mg/ml stock, LS-C204260, LifeSpan BioSciences, Inc.), the second antibody was *Hs*NR1D2 rabbit polyclonal antibody (dilution 1:500, HPA054798, Sigma-Aldrich). The following secondary antibodies and dilutions were used (1) Alexa Fluor® 647 AffiniPure Mouse Anti-Rabbit IgG (H+L) (Jackson ImmunoResearch Lab, Inc. cat # 211-605-109) (dilution 1:500) to stain *Hs*NR1D2 and (2) Alexa Fluor 488-conjugated AffiniPure donkey Anti-Goat IgG, Fc Fragment (Jackson ImmunoResearch Lab, Inc. #705-545-147) (dilution 1:1000) for 1 hour at room temperature.

After IFA staining, chambers were removed from *P. berghei*-infected Lab-Tek systems, slides were mounted with Vectashield with DAPI (Vector Labs), and #1.5 glass coverslips were affixed using nail polish. Images were acquired using a Zeiss LSM880 with Airyscan Confocal Microscope (63× oil immersion lens); with laser lines set to 3% for 405, 488, and 640 nm. The images were captured and processed using the confocal ZEN software (Blue and Black edition, Zeiss).The number of merozoites per schizont were counted using ImageJ software [61]

Isolation of RNA from uninfected hepatocytes and RNA sequencing—HC-04 shSCR and HC-04 sh*NR1D2* cells were plated in 6-well plates at a density of 300,000 cells per well. Forty-eight hours later, the cells were harvested from each well, pellets were washed with 1X PBS and stored at −80°C until further processing. Total RNA was isolated from the pellets of cells using RNeasy Plus Mini Kit (Qiagen, Cat# 74134), according to the manufacturer's protocol. Total RNA was assessed for quantity and quality using an Agilent Tapestation. RNA libraries were multiplexed and sequenced with 100 base pair (bp) paired end reads (PE100) to a depth of approximately 25 million reads per sample on an NovaSeq S4.

RNA Sequencing Analysis—Quality control of sequencing data was performed using FastQC (https://www.bioinformatics.babraham.ac.uk/projects/fastqc/). Raw reads were

preprocessed using Trimmomatic [62] and those with a length of 60 or more bases were kept. Filtered reads were then aligned to the human genome (GRch38, release 38) using STAR2.7.4a [63] and manually revised with IGV [64]. Gene expression quantification was calculated using RSEM1.3 [65]. Differential gene expression analysis was performed using DESeq2 [66] with standard settings. Over-represented genes were selected for enrichment analysis using Metascape [67].

Lipid droplet subcellular quantification in infected cells—Sixteen thousand cells per well of HC-04 shSCR and HC-04 sh*NR1D2* were individually seeded in poly L-lysine precoated 8-well chamber slides. Twenty-four hours later the cells were infected with *P. berghei* Luc sporozoites at a MOI of 1:1 (cells/sporozoites). At 48 hpi, the cells were fixed with 4% paraformaldehyde-PBS (Affymetrix) for 10 min at room temperature, permeabilized with 0.1% tritonX-100 (SIGMA) for 10 min at room temperature, blocked with 1% bovine serum albumin and stained overnight at 4 °C using antibody for UIS4 (*Plasmodium berghei* UIS4) goat polyclonal antibody (dilution 1:1000 from a 2 mg/ml stock, LS-C204260, LifeSpan BioSciences, Inc.). For visualizing *Pb*UIS4, Alexa Fluor 488-conjugated AffiniPure Goat Anti-Rabbit IgG, Fc Fragment (Jackson ImmunoResearch Lab, Inc. #111-545-046) (dilution 1:1000) was used to stain for 1 hour at room temperature. Following this, HCS LipidTOX™ Deep Red Neutral Lipid Stain (ThermoFisher Scientific Cat#: H34477) was added to the wells at a dilution of 1:500 for 30 mins at room temperature in dark. Chambers were then removed from *P. berghei*-infected Lab-Tek systems, slides, mounted with Vectashield with DAPI (Vector Labs), and #1.5 glass coverslips were affixed using nail polish. Images were acquired using a Zeiss LSM880 with Airyscan Confocal Microscope (63× oil immersion lens); with laser lines set to 3% for 405, 488, and 561nm. The images were captured and processed using the confocal ZEN software (Blue and Black edition, Zeiss).

To assess the effect of potential nuclear hormone receptor pathway modulating compounds on the lipid levels of the host, HC-04 cells were plated at a density of 16,000 cells/well in poly L-lysine precoated 8-well chamber slides. The cells were then pretreated with the test compounds: MMV1088447 and MMV1346624; and NR1D2 inhibitor ARN5187 at their IC_{50} and $2xIC_{50}$ concentrations, respectively, for 24 hours. Following this, the cells were infected with *P. berghei* Luc sporozoites at a MOI of 1:1 (cells/sporozoites). Compound treatment was further maintained for 48 hpi. Following this, the cells were fixed and processed for imaging as mentioned above. DMSO treated cells were used as negative control. MMV1088447 and MMV1346624 were purchased from MolPort. The purity of the compounds was assessed by LC-MS analysis. MMV1088447 had ~92% purity (Figure S6) and MMV1346624 had ~84% purity (Figure S7). ARN5187 was purchased from Millipore Sigma. The mean fluorescence intensity of lipid droplets in the infected cells and the treated cells was quantified using Image J software [61].

Statistical Analysis—The selection of candidate genes from the primary screen was conducted using the robust strictly standardized mean difference (robust SSMD). In addition, genes with p value < 0.05 as calculated by student' t-test were selected as 'hits.' RNA seq data was analyzed using DESeq2 v1.32.0 by estimating variance-mean

dependence in count data from high-throughput sequencing assays and test for differential expression based on a model using the negative binomial distribution and provides its own normalization approach. Data analyses were performed with GraphPad Prism (v8.3.0). Data shown in figures are averages of at least 2 replicates with standard error of means or are representative results of individual experiments. *p* values were stated in the figure legends. Sample size and statistical tests are also reported in the figure legends.

Supplementary Material

Refer to Web version on PubMed Central for supplementary material.

Acknowledgments

E.A.W. is supported by grants from the NIH (R01AI090141), the Bill and Melinda Gates Foundation (OPP1086217, OPP1141300, OPP1181458)., and Medicines for Malaria Venture. Image acquisition was done at UCSD Microscopy core supported by NINDS NS047101. RNA sequencing was done at UCSD Institute for Genomic Medicine Sequencing Core Facility. We would also like to thank UCSD Molecular Mass Spectrometry Facility for doing the LC-MS analysis of the compounds.

References

1. Mota MM, Hafalla JC, and Rodriguez A (2002). Migration through host cells activates Plasmodium sporozoites for infection. Nat Med 8, 1318–1322. 10.1038/nm785. [PubMed: 12379848]
2. Lindner SE, Miller JL, and Kappe SH (2012). Malaria parasite pre-erythrocytic infection: preparation meets opportunity. Cell Microbiol 14, 316–324. 10.1111/j.1462-5822.2011.01734.x. [PubMed: 22151703]
3. Meis JF, Verhave JP, Jap PH, Sinden RE, and Meuwissen JH (1983). Ultrastructural observations on the infection of rat liver by Plasmodium berghei sporozoites in vivo. J Protozool 30, 361–366. 10.1111/j.1550-7408.1983.tb02931.x. [PubMed: 6355454]
4. Vaughan AM, Mikolajczak SA, Wilson EM, Grompe M, Kaushansky A, Camargo N, Bial J, Ploss A, and Kappe SH (2012). Complete Plasmodium falciparum liver-stage development in liver-chimeric mice. J Clin Invest 122, 3618–3628. 10.1172/JCI62684. [PubMed: 22996664]
5. LaMonte GM, Orjuela-Sanchez P, Calla J, Wang LT, Li S, Swann J, Cowell AN, Zou BY, Abdel-Haleem Mohamed AM, Villa Galarce ZH, et al. (2019). Dual RNA-seq identifies human mucosal immunity protein Mucin-13 as a hallmark of Plasmodium exoerythrocytic infection. Nat Commun 10, 488. 10.1038/s41467-019-08349-0. [PubMed: 30700707]
6. De Niz M, Caldelari R, Kaiser G, Zuber B, Heo WD, Heussler VT, and Agop-Nersesian C (2021). Hijacking of the host cell Golgi by Plasmodium berghei liver stage parasites. J Cell Sci 134. 10.1242/jcs.252213.
7. Raphemot R, Toro-Moreno M, Lu KY, Posfai D, and Derbyshire ER (2019). Discovery of Druggable Host Factors Critical to Plasmodium Liver-Stage Infection. Cell Chem Biol 26, 1253–1262 e1255. 10.1016/j.chembiol.2019.05.011. [PubMed: 31257182]
8. Albuquerque SS, Carret C, Grosso AR, Tarun AS, Peng X, Kappe SH, Prudencio M, and Mota MM (2009). Host cell transcriptional profiling during malaria liver stage infection reveals a coordinated and sequential set of biological events. BMC Genomics 10, 270. 10.1186/1471-2164-10-270. [PubMed: 19534804]
9. Prudencio M, Rodrigues CD, Hannus M, Martin C, Real E, Goncalves LA, Carret C, Dorkin R, Rohl I, Jahn-Hoffmann K, et al. (2008). Kinome-wide RNAi screen implicates at least 5 host hepatocyte kinases in Plasmodium sporozoite infection. PLoS Pathog 4, e1000201. 10.1371/journal.ppat.1000201. [PubMed: 18989463]
10. Vijayan K, Arang N, Wei L, Morrison R, Geiger R, Parks KR, Lewis AJ, Mast FD, Douglass AN, Kain HS, et al. (2020). A Genome-wide CRISPR-Cas9 Screen Identifies Host Factors

Essential for Optimal Plasmodium Liver Stage Development. bioRxiv, 2020.2008.2031.275867. 10.1101/2020.08.31.275867.

11. Rodrigues CD, Hannus M, Prudencio M, Martin C, Goncalves LA, Portugal S, Epiphanio S, Akinc A, Hadwiger P, Jahn-Hofmann K, et al. (2008). Host scavenger receptor SR-BI plays a dual role in the establishment of malaria parasite liver infection. Cell Host Microbe 4, 271–282. 10.1016/j.chom.2008.07.012. [PubMed: 18779053]
12. Arang N, Kain HS, Glennon EK, Bello T, Dudgeon DR, Walter ENF, Gujral TS, and Kaushansky A (2017). Identifying host regulators and inhibitors of liver stage malaria infection using kinase activity profiles. Nat Commun 8, 1232. 10.1038/s41467-017-01345-2. [PubMed: 29089541]
13. Yang T, Ottilie S, Istvan ES, Godinez-Macias KP, Lukens AK, Baragana B, Campo B, Walpole C, Niles JC, Chibale K, et al. (2021). MalDA, Accelerating Malaria Drug Discovery. Trends Parasitol. 10.1016/j.pt.2021.01.009.
14. Antonova-Koch Y, Meister S, Abraham M, Luth MR, Ottilie S, Lukens AK, Sakata-Kato T, Vanaerschot M, Owen E, Jado JC, et al. (2018). Open-source discovery of chemical leads for next-generation chemoprotective antimalarials. Science 362. 10.1126/science.aat9446.
15. Gibson CC, Zhu W, Davis CT, Bowman-Kirigin JA, Chan AC, Ling J, Walker AE, Goitre L, Delle Monache S, Retta SF, et al. (2015). Strategy for identifying repurposed drugs for the treatment of cerebral cavernous malformation. Circulation 131, 289–299. 10.1161/CIRCULATIONAHA.114.010403. [PubMed: 25486933]
16. Gustafsdottir SM, Ljosa V, Sokolnicki KL, Anthony Wilson J, Walpita D, Kemp MM, Petri Seiler K, Carrel HA, Golub TR, Schreiber SL, et al. (2013). Multiplex cytological profiling assay to measure diverse cellular states. PLoS One 8, e80999. 10.1371/journal.pone.0080999. [PubMed: 24312513]
17. Rohban MH, Singh S, Wu X, Berthet JB, Bray MA, Shrestha Y, Varelas X, Boehm JS, and Carpenter AE (2017). Systematic morphological profiling of human gene and allele function via Cell Painting. Elife 6. 10.7554/eLife.24060.
18. Simm J, Klambauer G, Arany A, Steijaert M, Wegner JK, Gustin E, Chupakhin V, Chong YT, Vialard J, Buijnsters P, et al. (2018). Repurposing High-Throughput Image Assays Enables Biological Activity Prediction for Drug Discovery. Cell Chem Biol 25, 611–618 e613. 10.1016/j.chembiol.2018.01.015. [PubMed: 29503208]
19. Cuccarese MF, Earnshaw BA, Heiser K, Fogelson B, Davis CT, McLean PF, Gordon HB, Skelly K-R, Weathersby FL, Rodic V, et al. (2020). Functional immune mapping with deep-learning enabled phenomics applied to immunomodulatory and COVID-19 drug discovery. bioRxiv, 2020.2008.2002.233064. 10.1101/2020.08.02.233064.
20. Slack MD, Martinez ED, Wu LF, and Altschuler SJ (2008). Characterizing heterogeneous cellular responses to perturbations. Proc Natl Acad Sci U S A 105, 19306–19311. 10.1073/pnas.0807038105. [PubMed: 19052231]
21. Veschi V, Liu Z, Voss TC, Ozbun L, Gryder B, Yan C, Hu Y, Ma A, Jin J, Mazur SJ, et al. (2017). Epigenetic siRNA and Chemical Screens Identify SETD8 Inhibition as a Therapeutic Strategy for p53 Activation in High-Risk Neuroblastoma. Cancer Cell 31, 50–63. 10.1016/j.ccell.2016.12.002. [PubMed: 28073004]
22. Danovi D, Folarin A, Gogolok S, Ender C, Elbatsh AM, Engstrom PG, Stricker SH, Gagrica S, Georgian A, Yu D, et al. (2013). A high-content small molecule screen identifies sensitivity of glioblastoma stem cells to inhibition of polo-like kinase 1. PLoS One 8, e77053. 10.1371/journal.pone.0077053. [PubMed: 24204733]
23. Oppermann S, Ylanko J, Shi Y, Hariharan S, Oakes CC, Brauer PM, Zuniga-Pflucker JC, Leber B, Spaner DE, and Andrews DW (2016). High-content screening identifies kinase inhibitors that overcome venetoclax resistance in activated CLL cells. Blood 128, 934–947. 10.1182/blood-2015-12-687814. [PubMed: 27297795]
24. Bray MA, Singh S, Han H, Davis CT, Borgeson B, Hartland C, Kost-Alimova M, Gustafsdottir SM, Gibson CC, and Carpenter AE (2016). Cell Painting, a high-content image-based assay for morphological profiling using multiplexed fluorescent dyes. Nat Protoc 11, 1757–1774. 10.1038/nprot.2016.105. [PubMed: 27560178]

25. Meister S, Plouffe DM, Kuhen KL, Bonamy GM, Wu T, Barnes SW, Bopp SE, Borboa R, Bright AT, Che J, et al. (2011). Imaging of Plasmodium liver stages to drive next-generation antimalarial drug discovery. Science 334, 1372–1377. 10.1126/science.1211936. [PubMed: 22096101]
26. Leopold Wager CM, Arnett E, and Schlesinger LS (2019). Macrophage nuclear receptors: Emerging key players in infectious diseases. PLoS Pathog 15, e1007585. 10.1371/journal.ppat.1007585. [PubMed: 30897154]
27. Glennon EKK, Dankwa S, Smith JD, and Kaushansky A (2018). Opportunities for Host-targeted Therapies for Malaria. Trends Parasitol 34, 843–860. 10.1016/j.pt.2018.07.011. [PubMed: 30122551]
28. Franke-Fayard B, Janse CJ, Cunha-Rodrigues M, Ramesar J, Buscher P, Que I, Lowik C, Voshol PJ, den Boer MA, van Duinen SG, et al. (2005). Murine malaria parasite sequestration: CD36 is the major receptor, but cerebral pathology is unlinked to sequestration. Proc Natl Acad Sci U S A 102, 11468–11473. 10.1073/pnas.0503386102. [PubMed: 16051702]
29. Zhang XD (2011). Illustration of SSMD, z score, SSMD*, z* score, and t statistic for hit selection in RNAi high-throughput screens. J Biomol Screen 16, 775–785. 10.1177/1087057111405851. [PubMed: 21515799]
30. Yu M, Li W, Wang Q, Wang Y, and Lu F (2018). Circadian regulator NR1D2 regulates glioblastoma cell proliferation and motility. Oncogene 37, 4838–4853. 10.1038/s41388-018-0319-8. [PubMed: 29773903]
31. Solt LA, Wang Y, Banerjee S, Hughes T, Kojetin DJ, Lundasen T, Shin Y, Liu J, Cameron MD, Noel R, et al. (2012). Regulation of circadian behaviour and metabolism by synthetic REV-ERB agonists. Nature 485, 62–68. 10.1038/nature11030. [PubMed: 22460951]
32. Ramakrishnan SN, Lau P, Burke LJ, and Muscat GE (2005). Rev-erbbeta regulates the expression of genes involved in lipid absorption in skeletal muscle cells: evidence for cross-talk between orphan nuclear receptors and myokines. J Biol Chem 280, 8651–8659. 10.1074/jbc.M413949200. [PubMed: 15623503]
33. Tang M, Hu Z, Rao C, Chen J, Yuan S, Zhang J, Mao C, Yan J, Xia Y, Zhang M, et al. (2020). Burkholderia pseudomallei interferes with host lipid metabolism via NR1D2-mediated PNPLA2/ATGL suppression to block autophagy-dependent inhibition of infection. Autophagy, 1–16. 10.1080/15548627.2020.1801270. [PubMed: 31516068]
34. De Mei C, Ercolani L, Parodi C, Veronesi M, Lo Vecchio C, Bottegoni G, Torrente E, Scarpelli R, Marotta R, Ruffili R, et al. (2015). Dual inhibition of REV-ERBbeta and autophagy as a novel pharmacological approach to induce cytotoxicity in cancer cells. Oncogene 34, 2597–2608. 10.1038/onc.2014.203. [PubMed: 25023698]
35. Birth D, Kao WC, and Hunte C (2014). Structural analysis of atovaquone-inhibited cytochrome bc1 complex reveals the molecular basis of antimalarial drug action. Nat Commun 5, 4029. 10.1038/ncomms5029. [PubMed: 24893593]
36. LaMonte GM, Rocamora F, Marapana DS, Gnadig NF, Ottilie S, Luth MR, Worgall TS, Goldgof GM, Mohunlal R, Santha Kumar TR, et al. (2020). Pan-active imidazolopiperazine antimalarials target the Plasmodium falciparum intracellular secretory pathway. Nat Commun 11, 1780. 10.1038/s41467-020-15440-4. [PubMed: 32286267]
37. Helzer KT, Hooper C, Miyamoto S, and Alarid ET (2015). Ubiquitylation of nuclear receptors: new linkages and therapeutic implications. J Mol Endocrinol 54, R151–167. 10.1530/JME-14-0308. [PubMed: 25943391]
38. Mullard A (2019). Machine learning brings cell imaging promises into focus. Nat Rev Drug Discov 18, 653–655. 10.1038/d41573-019-00144-2. [PubMed: 31477870]
39. Pahl A, and Sievers S (2019). The Cell Painting Assay as a Screening Tool for the Discovery of Bioactivities in New Chemical Matter. Methods Mol Biol 1888, 115–126. 10.1007/978-1-4939-8891-4_6. [PubMed: 30519943]
40. Bray MA, Gustafsdottir SM, Rohban MH, Singh S, Ljosa V, Sokolnicki KL, Bittker JA, Bodycombe NE, Dancik V, Hasaka TP, et al. (2017). A dataset of images and morphological profiles of 30 000 small-molecule treatments using the Cell Painting assay. Gigascience 6, 1–5. 10.1093/gigascience/giw014.

41. Borges TK, Alves EA, Vasconcelos HA, Carneiro FP, Nicola AM, Magalhaes KG, and Muniz-Junqueira MI (2017). Differences in the modulation of reactive species, lipid bodies, cyclooxygenase-2, 5-lipoxygenase and PPAR-gamma in cerebral malaria-susceptible and resistant mice. Immunobiology 222, 604–619. 10.1016/j.imbio.2016.11.010. [PubMed: 27887739]
42. Mubaraki MA, Dkhil MA, Hafiz TA, Khalil MF, Al-Shaebi EM, Delic D, Elshaikh K, and Al-Quraishy S (2018). Vitamin D receptor regulates intestinal inflammatory response in mice infected with blood stage malaria. Microb Pathog 117, 299–303. 10.1016/j.micpath.2018.02.048. [PubMed: 29496525]
43. Raghuram S, Stayrook KR, Huang P, Rogers PM, Nosie AK, McClure DB, Burris LL, Khorasanizadeh S, Burris TP, and Rastinejad F (2007). Identification of heme as the ligand for the orphan nuclear receptors REV-ERBalpha and REV-ERBbeta. Nat Struct Mol Biol 14, 1207–1213. 10.1038/nsmb1344. [PubMed: 18037887]
44. Lam MT, Cho H, Lesch HP, Gosselin D, Heinz S, Tanaka-Oishi Y, Benner C, Kaikkonen MU, Kim AS, Kosaka M, et al. (2013). Rev-Erbs repress macrophage gene expression by inhibiting enhancer-directed transcription. Nature 498, 511–515. 10.1038/nature12209. [PubMed: 23728303]
45. Cho H, Zhao X, Hatori M, Yu RT, Barish GD, Lam MT, Chong LW, DiTacchio L, Atkins AR, Glass CK, et al. (2012). Regulation of circadian behaviour and metabolism by REV-ERB-alpha and REV-ERB-beta. Nature 485, 123–127. 10.1038/nature11048. [PubMed: 22460952]
46. Zhang Y, Fang B, Damle M, Guan D, Li Z, Kim YH, Gannon M, and Lazar MA (2016). HNF6 and Rev-erbalpha integrate hepatic lipid metabolism by overlapping and distinct transcriptional mechanisms. Genes Dev 30, 1636–1644. 10.1101/gad.281972.116. [PubMed: 27445394]
47. Liu DD, Han CC, Wan HF, He F, Xu HY, Wei SH, Du XH, and Xu F (2016). Effects of inhibiting PI3K-Akt-mTOR pathway on lipid metabolism homeostasis in goose primary hepatocytes. Animal 10, 1319–1327. 10.1017/S1751731116000380. [PubMed: 26956906]
48. Yecies JL, Zhang HH, Menon S, Liu S, Yecies D, Lipovsky AI, Gorgun C, Kwiatkowski DJ, Hotamisligil GS, Lee CH, and Manning BD (2011). Akt stimulates hepatic SREBP1c and lipogenesis through parallel mTORC1-dependent and independent pathways. Cell Metab 14, 21–32. 10.1016/j.cmet.2011.06.002. [PubMed: 21723501]
49. Liao X, Song L, Zhang L, Wang H, Tong Q, Xu J, Yang G, Yang S, and Zheng H (2018). LAMP3 regulates hepatic lipid metabolism through activating PI3K/Akt pathway. Mol Cell Endocrinol 470, 160–167. 10.1016/j.mce.2017.10.010. [PubMed: 29056532]
50. Le Martelot G, Claudel T, Gatfield D, Schaad O, Kornmann B, Lo Sasso G, Moschetta A, and Schibler U (2009). REV-ERBalpha participates in circadian SREBP signaling and bile acid homeostasis. PLoS Biol 7, e1000181. 10.1371/journal.pbio.1000181. [PubMed: 19721697]
51. Itoe MA, Sampaio JL, Cabal GG, Real E, Zuzarte-Luis V, March S, Bhatia SN, Frischknecht F, Thiele C, Shevchenko A, and Mota MM (2014). Host cell phosphatidylcholine is a key mediator of malaria parasite survival during liver stage infection. Cell Host Microbe 16, 778–786. 10.1016/j.chom.2014.11.006. [PubMed: 25498345]
52. Kluck GEG, Wendt CHC, Imperio GED, Araujo MFC, Atella TC, da Rocha I, Miranda KR, and Atella GC (2019). Plasmodium Infection Induces Dyslipidemia and a Hepatic Lipogenic State in the Host through the Inhibition of the AMPK-ACC Pathway. Sci Rep 9, 14695. 10.1038/s41598-019-51193-x. [PubMed: 31604978]
53. Rosenthal PJ (2021). Has artemisinin resistance emerged in Africa? Lancet Infect Dis 21, 1056–1057. 10.1016/S1473-3099(21)00168-7. [PubMed: 33864802]
54. Zumla A, Rao M, Wallis RS, Kaufmann SH, Rustomjee R, Mwaba P, Vilaplana C, Yeboah-Manu D, Chakaya J, Ippolito G, et al. (2016). Host-directed therapies for infectious diseases: current status, recent progress, and future prospects. Lancet Infect Dis 16, e47–63. 10.1016/S1473-3099(16)00078-5. [PubMed: 27036359]
55. Prudencio M, and Mota MM (2013). Targeting host factors to circumvent anti-malarial drug resistance. Curr Pharm Des 19, 290–299. 10.2174/138161213804070276. [PubMed: 22973886]
56. Posfai D, Maher SP, Roesch C, Vantaux A, Sylvester K, Peneau J, Popovici J, Kyle DE, Witkowski B, and Derbyshire ER (2020). Plasmodium vivax Liver and Blood Stages Recruit the Druggable Host Membrane Channel Aquaporin-3. Cell Chem Biol 27, 719–727 e715. 10.1016/j.chembiol.2020.03.009. [PubMed: 32330444]

57. Sonoda J, Pei L, and Evans RM (2008). Nuclear receptors: decoding metabolic disease. FEBS Lett 582, 2–9. 10.1016/j.febslet.2007.11.016. [PubMed: 18023286]
58. Marciano DP, Chang MR, Corzo CA, Goswami D, Lam VQ, Pascal BD, and Griffin PR (2014). The therapeutic potential of nuclear receptor modulators for treatment of metabolic disorders: PPARgamma, RORs, and Rev-erbs. Cell Metab 19, 193–208. 10.1016/j.cmet.2013.12.009. [PubMed: 24440037]
59. Dhangadamajhi G, and Singh S (2020). Sphingosine 1-Phosphate in Malaria Pathogenesis and Its Implication in Therapeutic Opportunities. Front Cell Infect Microbiol 10, 353. 10.3389/fcimb.2020.00353. [PubMed: 32923406]
60. Yalaoui S, Zougbede S, Charrin S, Silvie O, Arduise C, Farhati K, Boucheix C, Mazier D, Rubinstein E, and Froissard P (2008). Hepatocyte permissiveness to Plasmodium infection is conveyed by a short and structurally conserved region of the CD81 large extracellular domain. PLoS Pathog 4, e1000010. 10.1371/journal.ppat.1000010. [PubMed: 18389082]
61. Schneider CA, Rasband WS, and Eliceiri KW (2012). NIH Image to ImageJ: 25 years of image analysis. Nat Methods 9, 671–675. 10.1038/nmeth.2089. [PubMed: 22930834]
62. Bolger AM, Lohse M, and Usadel B (2014). Trimmomatic: a flexible trimmer for Illumina sequence data. Bioinformatics 30, 2114–2120. 10.1093/bioinformatics/btu170. [PubMed: 24695404]
63. Dobin A, Davis CA, Schlesinger F, Drenkow J, Zaleski C, Jha S, Batut P, Chaisson M, and Gingeras TR (2013). STAR: ultrafast universal RNA-seq aligner. Bioinformatics 29, 15–21. 10.1093/bioinformatics/bts635. [PubMed: 23104886]
64. Robinson JT, Thorvaldsdottir H, Winckler W, Guttman M, Lander ES, Getz G, and Mesirov JP (2011). Integrative genomics viewer. Nat Biotechnol 29, 24–26. 10.1038/nbt.1754. [PubMed: 21221095]
65. Li B, and Dewey CN (2011). RSEM: accurate transcript quantification from RNA-Seq data with or without a reference genome. BMC Bioinformatics 12, 323. 10.1186/1471-2105-12-323. [PubMed: 21816040]
66. Love MI, Huber W, and Anders S (2014). Moderated estimation of fold change and dispersion for RNA-seq data with DESeq2. Genome Biol 15, 550. 10.1186/s13059-014-0550-8. [PubMed: 25516281]
67. Zhou Y, Zhou B, Pache L, Chang M, Khodabakhshi AH, Tanaseichuk O, Benner C, and Chanda SK (2019). Metascape provides a biologist-oriented resource for the analysis of systems-level datasets. Nat Commun 10, 1523. 10.1038/s41467-019-09234-6. [PubMed: 30944313]

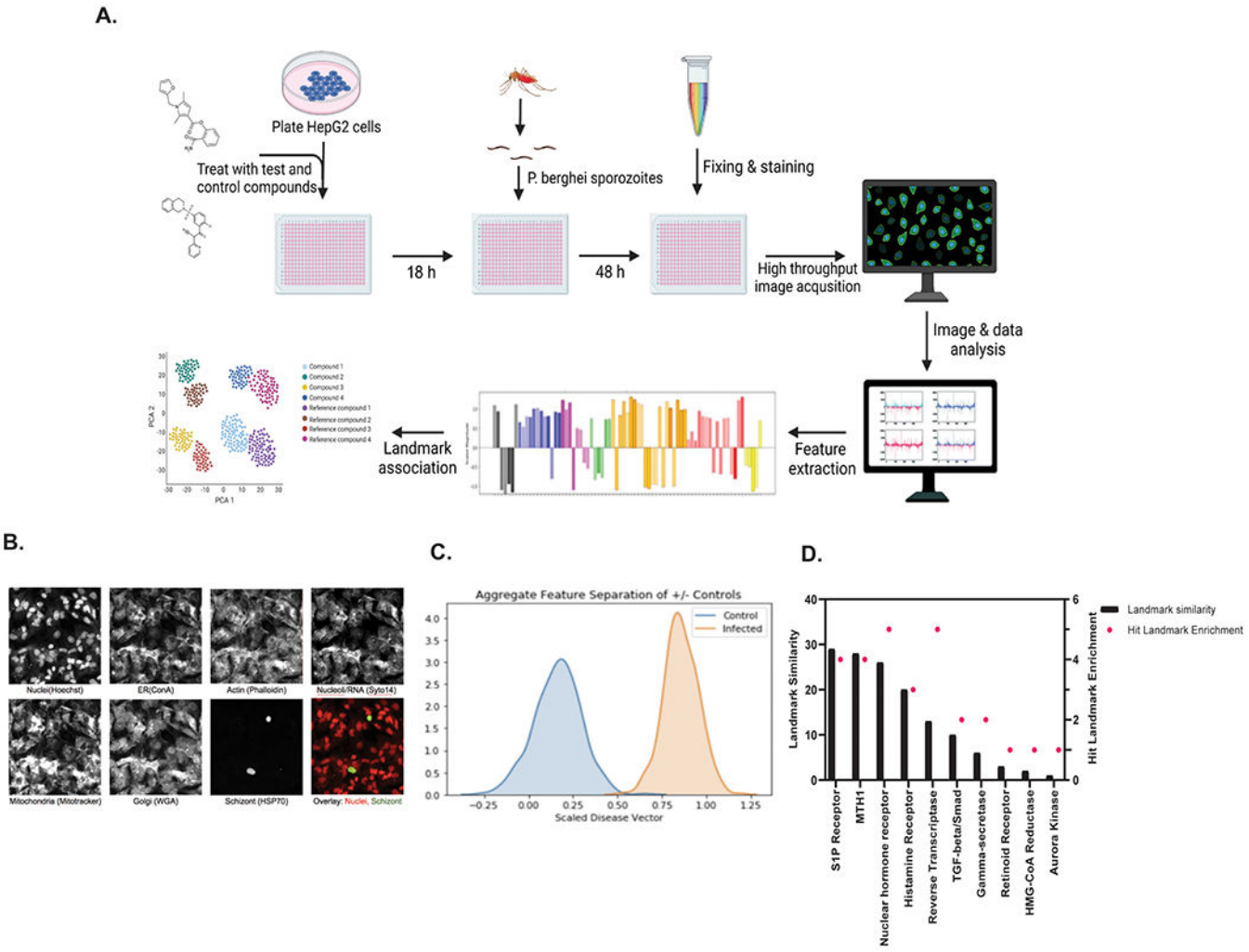

Figure 1: *Plasmodium* adapted Cell Painting assay applied to infected HepG2 cells identifies compounds that modulate host pathways.

(A) Morphological profiling of *Plasmodium* infected cellsOverview of the assay. 3000 HepG2 cells are were seeded in 384 multi-well plates. The cells were pretreated with the test antimalarials and reference compounds, respectively. Eighteen hours later cells were infected with *P. berghei* sporozoites at an MOI 1:3. Forty eight hours later cells were fixed. The cells were stained with different dyes and antibodies MitoTracker Deep Red, Hoechst 33342, Concanavalin A, SYTO 14 green fluorescent nucleic acid stain, Phalloidin, and wheat germ agglutinin. To visualize the schizonts *Py*HSP70 antibodywas used.. Images are acquired using ImageXpress MicroConfocal microscope. Each of 6 fluorescent channels were captured as an individual grayscale image. Using in-house deep learning algorithms, approximately 1000 morphological features were extracted from the acquired images using a deep convolutional neural network. These features were then used to create a phenoprint of the HepG2 cells treated with the test compound and compared with the profiles of those treated with reference compounds for pathway identification. Illustration was created with BioRender.com

(B) HepG2 cells 48-hours post *P. berghei* sporozoite infection labeled with Hoechst 33342, ConA, Syto14, Phalloidin, WGA, Mitotracker Deep Red, and mouse anti HSP70 (*P. berghei*). Cells exposed to healthy sporozoites were compared to those exposed to irradiated sporozoites (negative control) from the same parasite extraction at the same concentration of sporozoites/mL. See also Figure S1.

(C) A scaled (0-1), 1-dimensional projection of the positive (infected) and negative (irradiated) control populations illustrates the separability of the two classes in a representative experiment. This representation considers non-HSP70 features of the high dimensional space, with replicates aggregated (encompassing multiple sites for each well, and multiple wells that are sampled from the positive and negative control populations).

(D) Antimalarial compounds compared to 10 MoA profiles extracted from the Recursion Landmark Library. The number of compounds in each class is displayed in black (left axis) and pathways that show a class enrichment in the 72 hits highlighted in pink (right axis). See also Table S1, S2, S3 and S4.

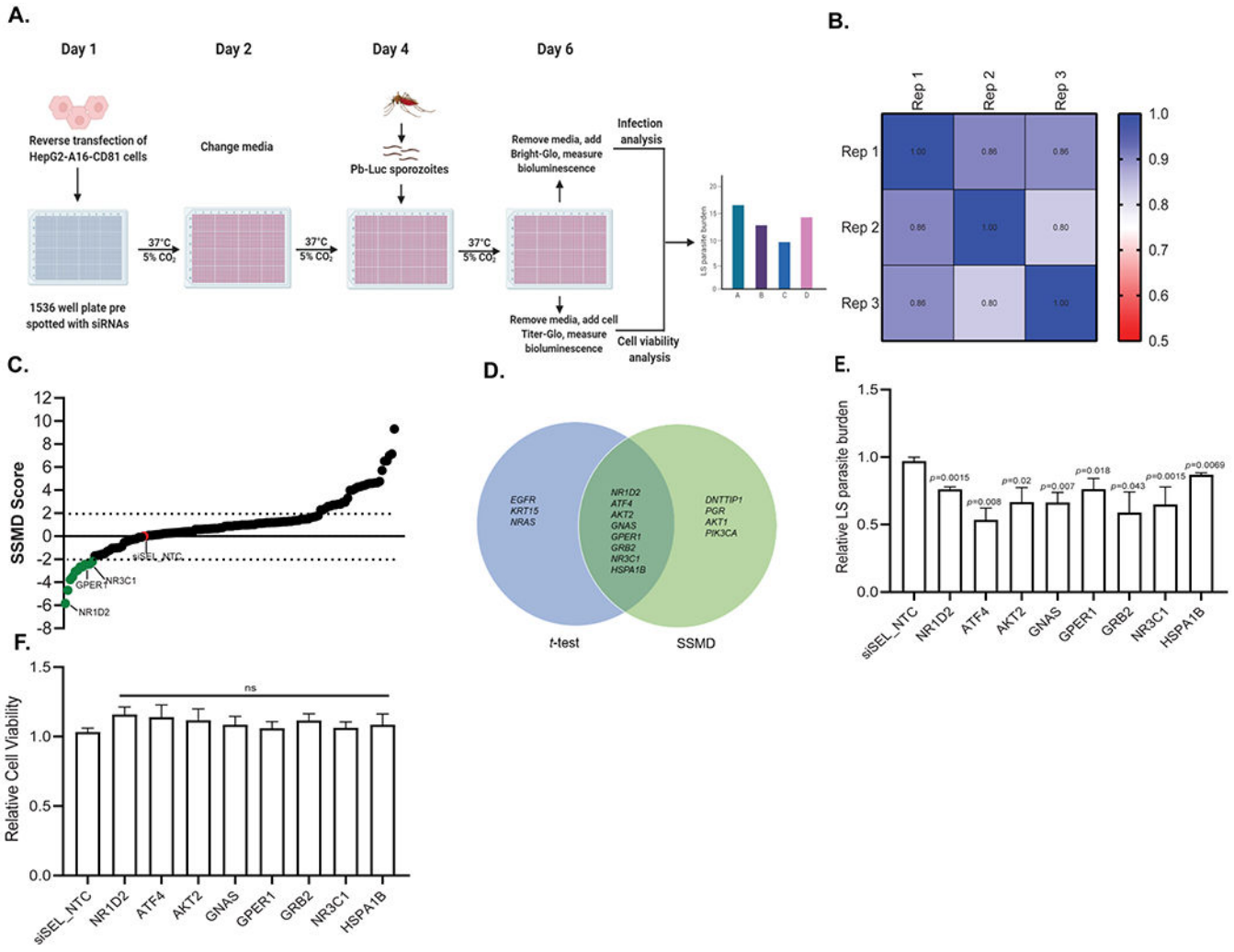

Figure 2: siRNA screen of NHR pathway members identifies host factors critical for *P. berghei* liver stage

(A) Schematic representation of the siRNA screenHepG2 cells were reverse tranfected with individual siRNAs in a 1536 well plate. Forty eight hours post siRNA transfection, *P. berghei* sporozoites expressing luciferase (Pb Luc) were added to the cells (MOI=0.3 and relative liver cell viability and parasite load were measured at forty eight hours post infection.. Illustration was created with BioRender.com. See also Table S5.

(B) Pearson correlation analysis of all three biological replicates. The r value was calculated using GraphPad Prism V 8.3.0.

(C) SSMD score analysis of 137 genes tested for reduction in Plasmodium liver stage infections. Genes highlighted in green represent those wherein knockdown had reduced infection with SSMD score ≤ −2. See also Table S6.

(D) Venn diagram of the genes that were identified as hits with two tailed t-tests and SSMD score analysis.

(E & F) Bar graph representing the relative infection leve€(E) and relative cell viability (F) in the eight genes that were identified as common hits between the two methods. The *p* value is indicated on top of each bar. Data represents Mean ± S.D.

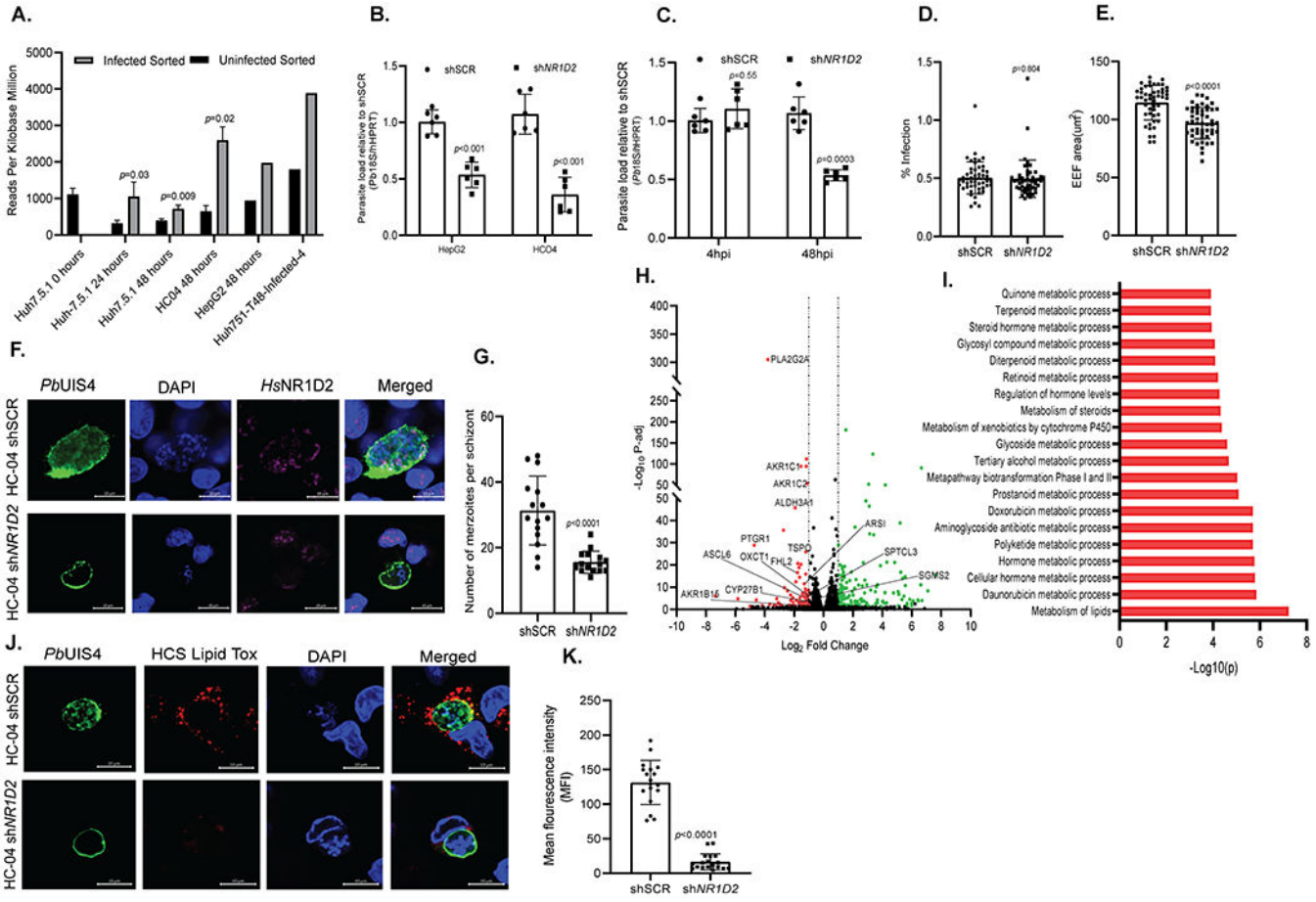

Figure 3: Knockdown of host *NR1D2* affects the intra-hepatic development of the schizonts.

(A) Reads per kilo base per million mapped reads (RPKM) of NR1D2 transcripts detected in infected sorted and uninfected sorted cells. The bars represent expression in indicated cells lines at varying time points. Statistical significance was calculated using GraphPad Prism V 8.3.0 (unpaired t-test).

(B) *P. berghei* infection levels (Pb18s/hhPRT) in HepG2 sh*NR1D2* and HC-04 sh*NR1D2* cell lines. Briefly, cells were infected with *P. berghei* sporozoites at a MOI of 1:2. Forty eight hours later, cells were harvested, total RNA was extracted and cDNA was synthesized to set up qRT PCR reactions. The infection levels were estimated by calculating the relative amounts of Pb 18s mRNA against the Hypoxanthine Guanine Phosphoribosyltransferase (HPRT) housekeeping gene. Data shown above represents mean ± S.D., with n=3 for HC-04 (G) cells and n=2 for HepG2 cells. Statistical significance was calculated using GraphPad Prism V 8.3.0 (unpaired students t-test).See also Figure S2, Table S7.

(C) Knockdown of NR1D2 does not impair the invasion of the host cells by the parasite, rather causes either developmental arrest or enhanced clearance of the parasite, *in vitro*.Briefly, HC-04 sh*NR1D2* and shSCR cells were infected with *P. berghei* sporozoites at a MOI of 1:2, cells were harvested at 4 hours and 48 hours post infection, RNA was extracted, and qPCR was set up. Infection level was estimated by calculating the relative amounts of Pb 18s mRNA against the Hypoxanthine Guanine Phosphoribosyltransferase (HPRT) housekeeping gene. The data shown above represents mean ± S.D., with n=2.

Statistical significance was calculated using GraphPad Prism V 8.3.0 (unpaired student's t-test).

(D & E) Percent infection (D) and the relative size of the EEFs (μM^2) (E) in HC-04 sh*SCR* and sh*NR1D2*. Cells wereinfected with *P. berghei* sporozoites at an MOI of 1:1. 48 hpi, cells were fixed, stained, and imaged using Operetta Confocal High Content Screening System. The percent infection and the size of the EEFs were determined as described in the methods section. Data shown represents two independent experiments (n=50). Statistical significance was calculated using GraphPad Prism V 8.3.0 (unpaired student's t-test, assuming unequal variance).

(F) Confocal microscopy images of representative HC-04 shSCR and sh*NR1D2* cells infected with *P. berghei* for 48 h.

Cells were labelled with *Hs*NR1D2 rabbit polyclonal antibody (dilution 1:500) and visualized using Alexa Fluor® 647 AffiniPure Mouse Anti-Rabbit IgG (H+L) (dilution 1:500) for host NR1D2. EEFs were stained using UIS4 (*Plasmodium berghei* UIS4) goat polyclonal antibody (dilution 1:1000 from a 2 mg/ml stock) and visualized using Alexa Fluor 488-conjugated AffiniPure Goat Anti-Rabbit IgG, (dilution 1:1000). DAPI (blue) was used to visualize the nuclei. Merged images for *Pb*UIS4, *Hs*NR1D2 and DAPI are shown. Scale bars represent 10 μM, 63x oil objective at zoom 4.

(G) Number of merozoites per schizont in HC-04 shSCR and sh*NR1D2* cells, respectively. The number of merozoites/ schizont in each cell line was counted using ImageJ software. The data represents two biological replicates (n=14). Statistical significance was calculated using GraphPad Prism V 8.3.0 (unpaired student's t-test, assuming unequal variance).

(H) Volcano plot of gene-expression pattern vs. *p* value. Genes with Log_2 fold change <−1 or >1 are highlighted in red and green, respectively. The position of genes specifically downregulated in the lipid metabolic pathways are indicated. See also Table S8, S9 and S10.

(I) Bar plot showing the enriched pathways for the genes downregulated in HC-04 sh*NR1D2* cells, relative to control shSCR cells. The x-axis indicates the enrichment significance ($-\log_{10}$ (*p* value) for each pathway term and the y-axis represents the GO term. Ordering is based on significance, with the bottom terms having the highest significance. See also Table S8, S9 and S10.

(J) Confocal microscopy images of representative HC-04 shSCR and sh*NR1D2* cells infected with *P. berghei* for 48 h. Cells were stained with HCS LipidTOX (dilution 1:500) to visualize the lipid droplets. EEFs were stained using UIS4 (*Plasmodium berghei* UIS4) goat polyclonal antibody (dilution 1:1000 from a 2 mg/ml stock) and visualized using Alexa Fluor 488-conjugated AffiniPure Goat Anti-Rabbit IgG, (dilution 1:1000). DAPI (blue) was used to visualize the nuclei.Merged images for *Pb*UIS4, HCS LipidTox and DAPI are shown. Scale bars represent 10 μM, 63x oil objective at zoom 4. See also Figure S3

(K) Mean fluorescence intensity (MFI) of the lipid droplets in HC-04 shSCR and sh*NR1D2* cells infected with *P. berghei* for 48 h. The MFI for each infected field was counted using ImageJ software. The data represents two biological replicates (n=17). Statistical significance was calculated using GraphPad Prism V 8.3.0 (unpaired student's t-test, assuming unequal variance).

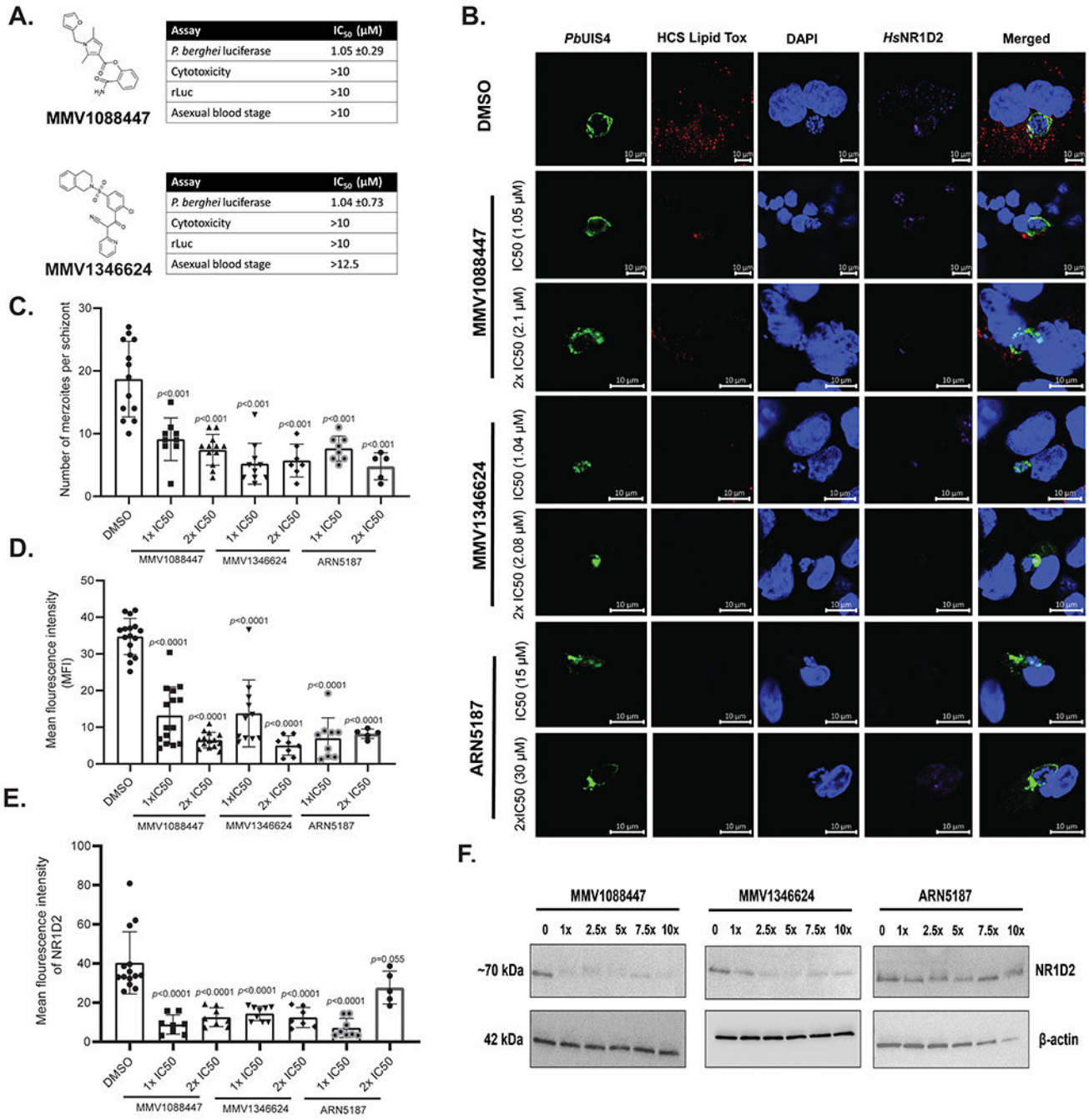

Figure 4: NHR modulating compounds phenocopy NR1D2 knockdown in host cells

(A) Chemical structures of MMV1088447 and MMV1346624, that were identified as potential nuclear hormone receptor modulating compounds. The IC_{50} values of these compounds in *P. berghei* luciferase, cytotoxicity, recombinant luciferase (rLuc) and asexual blood stage assays are mentioned. See also Figure S6 and S7.

(B) Confocal microscopy images of *P. berghei* infected HC-04 cells treated with DMSO, MMV1088447, MMV1346624 and ARN5187, respectively, for 48h. HC-04 cells were pretreated with the mentioned concentrations of each test and control compound. Pretreated

cells were infected 24 hours later with *P. berghei* sporozoites. 48 hpi, cells were fixed and processed for imaging. Cells were labelled with *Hs*NR1D2 rabbit polyclonal antibody (dilution 1:500) and visualized using Alexa Fluor® 647 AffiniPure Mouse Anti-Rabbit IgG (H+L) (dilution 1:500) for host NR1D2. HCS LipidTOX (dilution 1:500) was used to visualize the lipid droplets. EEFs were stained using UIS4 (*Plasmodium berghei* UIS4) goat polyclonal antibody (dilution 1:1000 from a 2 mg/ml stock) and visualized using Alexa Fluor 488-conjugated AffiniPure Goat Anti-Rabbit IgG, (dilution 1:1000). DAPI (blue) was used to visualize the nuclei.Merged images for *Pb*UIS4, HCS LipidTox, DAPI and *Hs*NR1D2 are shown. Scale bars represent 10 μM, 63x oil objective at zoom 4. See also Figure S4 and S5.

(C) Number of merozoites per schizont in HC-04 cells treated with DMSO, MMV1088447, MMV1346624 and ARN5187, respectively, for 48h. The number of merozoites/schizont was counted using ImageJ software. The data represents two biological replicates. Statistical significance was calculated using GraphPad Prism V 8.3.0 (One way ANOVA, Dunnett's multiple comparisons test).

(D) Mean fluorescence intensity (MFI) of the lipid droplets in HC-04 cells treated with DMSO, MMV1088447, MMV1346624 and ARN5187, respectively, for 48h. The MFI for each infected field was counted using ImageJ software. The data represents two biological replicates. Statistical significance was calculated using GraphPad Prism V 8.3.0 (One way ANOVA, Dunnett's multiple comparisons test).

(E) Mean fluorescence intensity (MFI) of the NR1D2 in HC-04 cells treated with DMSO, MMV1088447, MMV1346624 and ARN5187, respectively, for 48h. The MFI for each infected field was counted using ImageJ software. The data represents two biological replicates. Statistical significance was calculated using GraphPad Prism V 8.3.0 (One way ANOVA, Dunnett's multiple comparisons test).

(F) Relative expression levels of NR1D2 in uninfected HC-04 cells treated with the indicated concentrations of MMV1088447, MMV1346624 and ARN5187, respectively, for 48h. Post treatment cells were lysed and the expression levels of HsNR1D2 was analyzed using *Hs*NR1D2 rabbit polyclonal antibody. B actin was used as loading control.

Table 1:

List of genes, Protein name and GO annotations of the genes identified as hits

Gene Name	Protein Name	Biological Process GO Annotations
AKT2	AKT serine/threonine kinase 2	GO:1901653 GO:0032869 GO:0042221 GO:1903426 GO:0050790
ATF4	Activating transcription factor 4	GO:0006984 GO:0036499 GO:0034976 GO:0042594 GO:0030968
GNAS	Guanine Nucleotide Binding Protein (G Protein), Alpha Stimulating	GO:0007189 GO:0007186 GO:0071417 GO:0007191 GO:0032870
GPER1	G Protein-Coupled Estrogen Receptor 1	GO:0007187 GO:0007193 GO:0007188 GO:0007186 GO:0008015
GRB2	Growth Factor Receptor Bound Protein 2	GO:0038128 GO:0038127 GO:0007169 GO:0007173 GO:0009967
HSPA1B	Heat Shock Protein Family A (Hsp70) Member 1B	GO:0006457 GO:1900034 GO:0009408 GO:0042026 GO:0090083
NR1D2	Rev ERB beta (Nuclear Receptor Subfamily 1 Group D Member 2)	GO:0048511 GO:0032922 GO:0007623 GO:0042752 GO:0045892
NR3C1	Glucocorticoid receptor (Nuclear receptor subfamily 3 group C member 1)	GO:0048511 GO:1900034 GO:0007623 GO:0030522 GO:0030518